Russian Geology and Geophysics © 2024, Novosibirsk State University
Available online in April, pp. 1–18, 2024 *DOI:10.2113/RGG20244705* *Geologiya i Geofizika*

Granulites of the Larba Block of the Dzhugdzhur–Stanovoi Superterrane: Reconstruction of the Formation Conditions

Sh.K. Baltybaev[a,b,] ✉, D.V. Dolivo-Dobrovolsky[a], A.V. Yurchenko[a], Yu. R. Volkova[c], E.S. Malchushkin[c]

[a]*Institute of Precambrian Geology and Geochronology, Russian Academy of Sciences, nab. Makarova 2, St. Petersburg, 199034, Russia*

[b]*St. Petersburg State University, Institute of Geosciences, Universitetskaya nab. 7, St. Petersburg, 199034, Russia*

[c]*OSP Amurgeologiya AO Dal'nevostochnoe Proizvodstvenno-Geologicheskoe Ob"edinenie, per. Chudinovskii 15, Blagoveshchensk, 675000, Russia*

Received 20 November 2023; accepted 30 January 2024

Abstract—We discuss the rocks of the Larba granulite block in the Ilikan zone of the Dzhugdzhur–Stanovoi superterrane. The Larba block is dominated by basic schists and garnet–biotite–orthopyroxene and garnet–biotite–cordierite–sillimanite gneisses (metabasites and metapelites). Calculation of temperatures and pressures of mineral formation was carried out by multi-equilibrium geothermobarometry, which makes it possible to evaluate the degree of equilibrium of mineral compositions along with *P–T* parameters. The *P–T* estimates have shown metamorphism of aluminous gneisses under moderate-pressure granulite facies conditions (7–8 kbar, 800–850 °C). Orthopyroxene granulites formed under granulite-amphibolite transition facies conditions. The mineral compositions and parageneses in highly ferrous metabasites permitted estimation of the conditions of metamorphism, P = 4–5 kbar and T = 630–700 °C, and show no influence of earlier granulite facies metamorphism. The bimodal *P–T* distribution for most samples of aluminous gneisses most probably reflects progressive and near-peak conditions of granulite metamorphism. The time of enderbite magmatism is determined from the upper intercept of discordia with concordia at 2546 ± 52 Ma and should be verified. The age of metamorphic rims over enderbite zircon is 1882 ± 11 Ma. The model Nd age of enderbites, T^{Nd}(DM) = 2.57–2.58 Ga, is close to the age of the core of enderbite zircon and differs significantly from the model Nd age of the host metamorphic rocks (2.8–3.0 Ga). The Paleoproterozoic metamorphism of the Larba block rocks regionally coincides with the third stage of collisional granitoid magmatism of the southeastern Siberian craton and records the formation of this structure.

Keywords: Larba block; Aldan Shield; granulites; *P–T* parameters; enderbites; age; metamorphism

INTRODUCTION

The geologic structure and evolution of the Dzhugdzhur–Stanovoi superterrane in the northeast of the Central Asian Orogenic Belt are the subjects of many studies and discussions (Kastrykina, 1983; Kozyreva et al., 1985; Moskovchenko et al., 1985; Sedova and Glebovitskii, 1985; Aleksandrov and Avchenko, 2002; Glebovitsky et al., 2009; Kotov et al., 2014; Velikoslavinskii et al., 2017). One of the key issues of scientific disagreement is the nature of granulite blocks, which are not numerous (occupying no more than 5% of the superterrane area) but are of great importance for understanding the structure and tectonic evolution of the entire Dzhugdzhur–Stanovoi folded area. There are two viewpoints of the nature of the granulite rocks of these blocks: (1) These are highs of the ancient basement on which the protoliths of the metamorphic rocks of the Stanovoi Complex formed (Dzevanovskii, 1958); (2) The granulites are "outliers" preserved during intense low-temperature metamorphism of the rocks of the Stanovoi Complex (Korzhinskii, 1936). Based on the recently obtained geochronological and isotope-geochemical data, it was assumed that the granulites of the Dzhugdzhur–Stanovoi folded area might be deep parts of the so-called "Ilikan unit", which were exhumed during the closure of the Mongol–Okhotsk Ocean in the Mesozoic (Velikoslavinskii et al., 2017). Earlier U–Pb geochronological studies of detrital zircons determine the age of the Ilikan unit in the interval 2630–2700 Ma (Velikoslavinskii et al., 2011).

The paper considers the rocks of one of the granulite blocks, Larba, which is part of the structures of the Ilikan zone of the Dzhugdzhur–Stanovoi superterrane (Fig. 1). To refine the composition and conditions of formation of the Larba block granulites, we attempted to estimate the *P–T* parameters of rock metamorphism by other isotope-geochemical and geochronological studies. The main goal of our research is the detailed description of the conditions of formation of the Larba block granulites and the geochrono-

✉ Corresponding author.
E-mail address: shauket@mail.ru (Sh.K. Baltybaev)

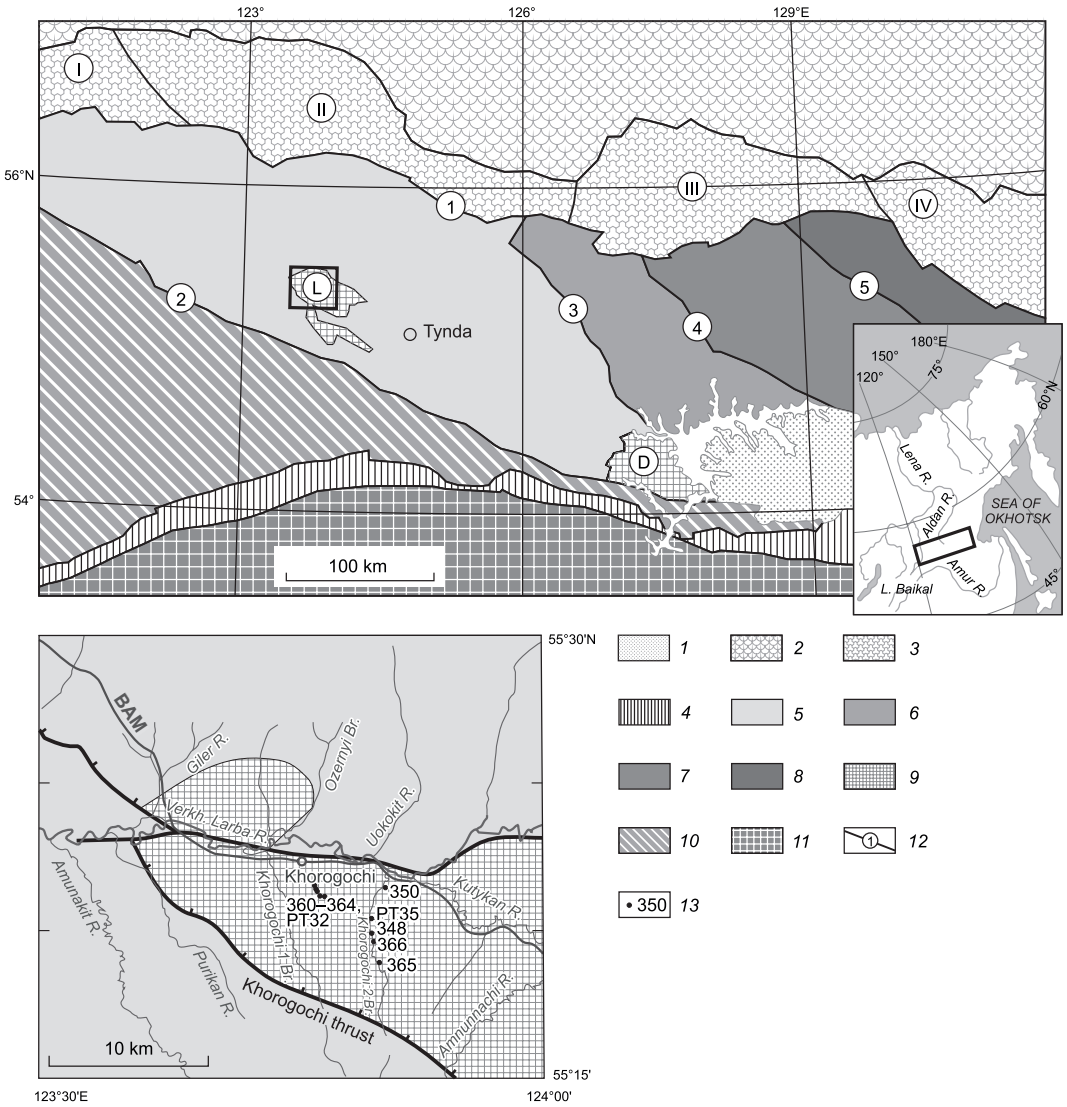

Fig. 1. Schematic map of tectonic zoning of the western Dzhugdzhur–Stanovoi superterrane of the Central Asian Orogenic Belt (Velikoslavinskii et al., 2017). *1* – Zeya depression; *2* – Aldan Shield; *3* – Stanovoi structural suture: Kurul'ta block (I), Zverevo block (II); Sutam block (III), Ayumkan block (IV); *4* – Mongol–Okhotsk Orogenic Belt; *5–8* – structure-formation zones of the Dzhugdzhur–Stanovoi superterrane: *5* – Ilikan, *6* – Bryanta, *7* – Kupuri, *8* – Zeya; *9* – granulite blocks of the Ilikan zone: L – Larba, D – Dambuki; *10* – Selenga-Stanovoi superterrane; *11* – Amur microcontinent; *12* – major faults: 1 – Stanovoi, 2 – Dzheltulak, 3 – Unakha, 4 – Sugdzhar, 5 – Taksakanda; *13* – sampling localities (in the inset and in the magnified part of the figure). BAM – Baikal-Amur Mainline.

logical estimation of the time of manifestation of granulite metamorphism and enderbite magmatism. We attempted to reconstruct the stages of rock metamorphism in order to integrate these results into the most adequate tectonic model for the evolution of the regional granulite complexes.

A GEOLOGICAL OVERVIEW OF THE LARBA BLOCK AND THE PERIODICITY OF METAMORPHIC EVENTS WITHIN THE DZHUGDZHUR–STANOVOI SUPERTERRANE

In the Ilikan zone of the Dzhugdzhur–Stanovoi superterrane, the Larba and Dambuki blocks were identified. Their rocks (biotite, biotite–garnet, hypersthene gneisses, and two-pyroxene schists) are tentatively (without required geochronological substantiation) assigned to the Paleoarchean Larba and Dambuki groups, respectively (Glukhovskii and Sintserova, 1979).

The Larba block is dominated by basic schists, but garnet–biotite–orthopyroxene and garnet–biotite–cordierite–(sillimanite) gneisses are also present. These rocks are part of riders of recumbent isoclinal folds and associated subhorizontal shear zones (Glebovitskii et al., 2009). The development of these structures was followed by the formation of enderbite–gneisses, charnockite–gneisses, and, somewhat later, vein charnockite and enderbite bodies (Glebovitskii et al., 2009).

The metamorphosed and migmatized (under granulite facies conditions) rocks of the Larba block are intruded by bodies of metamorphosed gabbroids, anorthosites, and enderbites (Moskovchenko et al., 1985; Sedova and Glebovitskii, 1985). Some of them were dated: the Khorogochi gabbro-anorthosite massif (2633 ± 20 Ma) intruding the rocks of the Larba block; the Maristyi olivinite–websterite–gabbro massif (2643 ± 31 Ma, LA-ICP-MS zircon U–Th–Pb dating) (Buchko et al., 2008) intruding the rocks of the Ilikan unit; and tectonic metagabbro sheets (2635 ± 4 Ma, ID-TIMS zircon U–Pb dating) (Velikoslavinskii et al., 2011) in the Ilikan unit.

The Dzhugdzhur–Stanovoi superterrane, including the Ilikan zone and granulite blocks, is composed of polymetamorphic rocks. The time of the most ancient metamorphic event in the Ilikan zone is estimated at 2760 ± 15 Ma (Velikoslavinskii et al., 2017). The tectonic processes that caused this event are unknown.

The Proterozoic metamorphic event in the Bryanta zone was, most likely, caused by the collision of terranes corresponding to the Ilikan and Zeya zones, ca. 1.9 Ga. Nearly coeval metamorphism (1961 ± 16 Ma) is also assumed for the rocks of the Zeya zone (Velikoslavinskii et al., 2017). Taking into account the uncertainties of dating, we think it was the same metamorphic event. Although the area of its manifestation is not precisely known, it might include the rocks of the Ilikan zone.

The last metamorphic events in this region took place much later than the two previous ones. Available data indicate that the rocks of the Dzhugdzhur–Stanovoi terrane underwent high-temperature structural and metamorphic transformations in the Mesozoic, ca. 140 Ma (Larin et al., 2006), as a result of the closure of the Mongol–Okhotsk Ocean.

METHODS AND MATERIALS

During the short-term field work (2019), we examined the granulite strata of the Larba block in the area of the Srednyaya (Middle) Larba River basin (Fig. 1) and sampled their rocks for petrological, isotope-geochemical, and geochronological studies. The main attention was focused on the mineralogical and petrological characteristics of metamorphic rocks and the reconstruction of the formation conditions of the Larba block granulites. The samples from metapelite and metabasite strata (a total of 42 samples) were studied in most detail; they were used to prepare specimens for the analyses described below.

Microprobe studies of minerals in polished sections were carried out using a JSM-6510LA scanning electron microscope with a JED-2200 JEOL energy-dispersive spectrometer (Institute of Precambrian Geology and Geochronology RAS, St. Petersburg). Operating conditions: accelerating voltage 20 kV, current 1 nA, and ZAF correction of matrix effects. Natural minerals and pure oxides and metals were used as standard samples. The detection limit of the elements to be determined was 0.1%. Representative local sites 2–3 mm in size were marked during petrographic examination of the polished thin sections, within which analyses of the closely spaced mineral grains were then carried out at several points per grain for a more detailed description of chemical variations.

Contents of chemical elements in the rocks were determined by the X-ray fluorescence (XRF) method at the Karpinsky All-Russian Research Geological Institute, St. Petersburg. The analysis was carried out in fused 4 g pellets prepared by mixing of 50% lithium metaborate and 50% lithium tetraborate in the ratio of 1:9 and the subsequent melting of this flux in gold–platinum crucibles and pressing. The detection limit of oxides was 0.01–0.03 wt.%, and that of trace elements, 2–5 ppm.

Inductively coupled plasma mass spectrometry (ICP MS) was used for a multielement analysis of both major components and trace elements in rocks. Powdered samples were transferred into solution and digested with a mixture of acids, or the alloy of powdered samples with flux (lithium metaborate or tetraborate) was subjected to acid digestion. The sample fusion was performed in muffle furnaces and platinum or graphite crucibles. The analysis was carried out on mass spectrometers with an additional quadrupole system to reduce the background and decrease the detection limits of elements. The lower ICP MS detection limits for various chemical elements were 0.0005–0.08 ppm.

U–Th–Pb *isotope studies* (SHRIMP-II) and U and Pb isotope analysis were performed on a SHRIMP-II secondary ion microprobe at the Center of Isotopic Research (CIR) of the A.P. Karpinsky Russian Geological Research Institute RAS, St. Petersburg. The points for isotope analysis were chosen based on cathodoluminescence (CL) and back-scattered electron (BSE) images of zircon crystals. The analyzed site of zircon crystals measured ca. 20 μm. The analytical data were processed according to Williams' (1997) technique, using the Squid-1.13a (Ludwig, 2005) and Isoplot-3.75 (Ludwig, 2012) software. The Pb/U ratio in zircon was normalized to a $^{206}Pb/^{238}U$ value of 0.0665 in the Temora zircon standard (Black et al., 2004). The contents of lead, uranium, and thorium were determined relative to the 91500 standard zircon with a known uranium content (Wiedenbeck et al., 1995).

Analysis for Sm *and* Nd *in rocks* was carried out by the isotope dilution method at the CIR. Weighed amounts of solutions of mixed ^{149}Sm–^{150}Nd indicators were added to 100–150 mg ground samples. Then, the samples were digested in a HNO_3 + HF mixture. Samarium and neodymium for isotope analysis were separated in two stages: first, by cation exchange chromatography, using an AG50W-X8 resin to separate REE from the bulk mass of rocks and minerals, and then, by extraction chromatography, using an HDEHP liquid cation exchange extraction agent applied to a Teflon support. A Sm and Nd isotope analysis was carried out on a TRITON nine-collector mass spectrometer in static mode. Correction for Nd isotope fractionation was made by

normalizing the measured values to $^{148}Nd/^{144}Nd = 0.241578$. The normalized isotope ratios were reduced to the $^{143}Nd/^{144}Nd$ value of 0.511860 in the La Jolla International isotope standard. The error of determination of the Sm and Nd content was 0.5%.

The temperature and pressure of mineral formation were determined by multi-equilibrium geothermobarometry, which makes it possible to evaluate both the *P–T* parameters of mineral formation and the degree to which the mineral compositions approach equilibrium. The winTWQ software (Berman, 1991), version 2.64, with the DEC06 (Berman, 2007) and BA96A (Berman and Aranovich, 1996) thermodynamic databases was used. In addition, phase diagrams (pseudosections) were constructed for the certain bulk chemical composition of the system, using the GeoPS software, version 3.3 (Xiang and Connolly, 2022), with the DS622 thermodynamic database (Holland and Powell, 2011) and solid solution and melt models (Green et al., 2016) elaborated for the system $MnO–TiO_2–Na_2O–CaO–K_2O–FeO–MgO–Al_2O_3–SiO_2–H_2O–CO_2–O_2$.

In this research we applied the *permutational multi-equilibrium geothermobarometry* method, which implies using all possible combinations of the compositions of closely spaced grains of minerals assumed to be in equilibrium. With this approach, we obtained an array of points in the *P–T* diagram, which limits the field with all probable pressure and temperature values for the used mineral compositions. Such an approach is necessary because a thorough study of the mineral composition often shows their significant chemical heterogeneity within even minor (few millimeters) local sites of the rock. It is obvious that the choice of such mineral compositions affects crucially the geothermobarometry results. It is important that multi-equilibrium geothermobarometry permits estimating the degree of equilibrium of the mineral compositions under study. As the mineral compositions approach the equilibrium ones, the lines of all reactions tend to intersect at a single point in the *P–T* diagram. Thus, each of the *P–T* points in the diagram has a third numerical parameter, which reflects the degree of convergence of the mineral reaction lines.

The heterogeneity of mineral compositions cannot be treated as statistical or systematic analytical errors because of the regularity of detected variations determined by the rock structure specifics, i.e., the relationship of the rock grains with the environment. This specific feature depicts a significant drawback of the statistical approach used in geothermobarometry, in which variations in mineral composition are simulated by the Monte Carlo method (Lieberman and Petrakakis, 1991). This method simulates random compositions following a normal distribution around some chosen composition, whereas real composition variations are closer to vectors, i.e., show strong correlations. This is best evident in the case of chemical zoning of mineral (e.g., garnet) grains.

The established regularities of variations in mineral compositions might be due to both the initial local chemical heterogeneity of the substrate and the specifics of mineral formation. Some regularities can be explained by simple models, e.g., postcrystallizational diffusion exchange, fractionation of elements during the grain growth, or superposed transformations. However, these models are speculative and admit the existence of alternative mechanisms. It is usually difficult to determine which mineral compositions should correspond to the thermodynamic (chemical) equilibrium ones. Using the above-described permutational method does not rule out the common approach to the choice of mineral compositions for geothermobarometry, based on analysis of structural relations. Moreover, study of the structures and textures of rocks in thin sections and the following choice of mineral compositions can significantly reduce the domains of uncertainty of *P–T* parameters.

The combination method was implemented using the TWQ_Comb (Dolivo-Dobrovolsky, 2006a) and TWQ_View (Dolivo-Dobrovolsky, 2006b) software being wrappers of the winTWQ software (Berman, 2007). As a measure of the convergence of the equilibrium lines, the mean-square distance (MSD) from all reaction lines to the *P–T* point of interest is used. The dimensionless MSD value is numerically equal to the temperature difference due to scaling of only the pressure axis (kbar) with a constant factor of 50. The better the convergence of the lines in the diagram, the lower the MSD value. The points of the average *P–T* parameters are determined by searching for the minimum MSD value. Note that there is no clear answer to the question at what MSD values the determination of *P–T* parameters should be considered satisfactory: This is decided subjectively based on a visual analysis of the arrangement of the reaction lines in the diagrams.

PETROGRAPHY OF THE STUDIED ROCKS

We have identified two groups of the studied rocks, metabasites and metapelites, which differ strongly from each other in chemical and mineral compositions (Figs. 2 and 3, Table 1; Supplementary Materials, Table ESM_1). We also examined enderbites (igneous rocks) and determined their U–Th–Pb and Sm–Nd isotopic ages. In addition, we studied one of the granulite samples, orthopyroxene–biotite–garnet gneiss, which differs significantly in chemical composition from the samples of the above groups.

Metapelites (aluminous gneisses) are rocks with a gneissose, often banded or spotted–banded structure due to migmatization widely manifested in some samples. The melanosome is formed by clusters of porphyroblasts of garnet, biotite, and other aluminous minerals, and the leucosome has a predominantly garnet–plagioclase–quartz composition. The rocks have inequigranular, lepidogranoblastic, lepidonematogranoblastic, and porphyroblastic textures. A typical mineral assemblage is Grt + Bt ± Sil ± Crd ± Kfs + Pl + Qz[1] (Fig. 3*a*), whereas cordierite is found only within

[1] Mineral abbreviations are after Warr (2021).

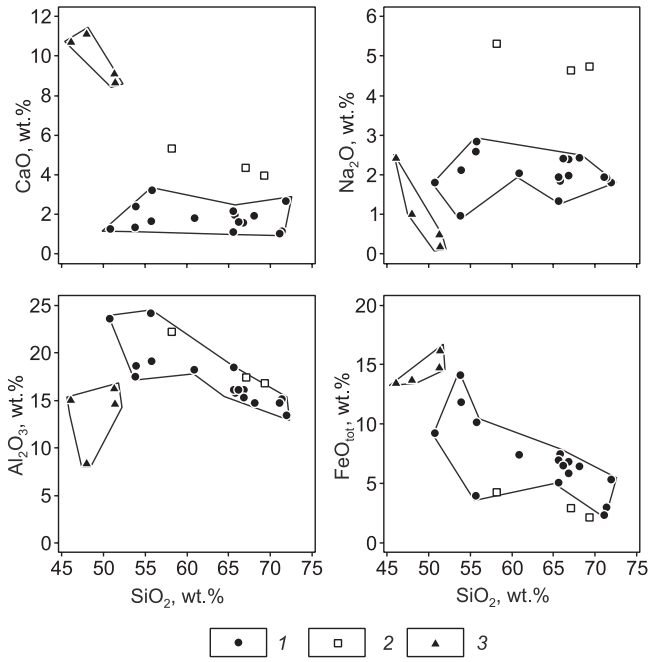

Fig. 2. Major-element diagrams for the studied rocks of the Larba block. *1* – metapelites; *2* – enderbites; *3* – metabasites.

narrow (1–2 mm) elongate zones of superposed schistosity with the partial resorption of adjacent garnet porphyroblasts (often with coronas of cordierite–quartz symplectite intergrowths). These zones also contain secondary biotite, which often forms symplectite intergrowths with quartz. The accessory minerals are ilmenite, rutile, and zircon; also, spinel as part of a polymineral inclusion in garnet was found (Fig. 4*a*). In most samples, late diaphthoresis is manifested to varying degrees as the formation of late biotite, muscovite, and chlorite (Figs. 3*f* and 4*d*) and as pinitization of cordierite.

Orthopyroxene–biotite–garnet gneiss (sample 359-2) is a rock with a gneissose, often banded structure due to migmatization and an equigranular nematogranoblastic texture. The melanosome is formed by a fine-grained (0.5–1.5 mm) orthopyroxene–plagioclase aggregate with scarce ilmenite and quartz grains. Along the contacts with the leucosome in a ca. 10 mm thick zone, the melanosome is enriched with garnet, biotite, and quartz grains (Fig. 3*e*). The up to 1–2 cm thick leucosome bands are characterized by a high content of feldspars and quartz, whose grains are several times larger than those in the melanosome. The dark-colored minerals in the leucosome are garnet and biotite. K-feldspar occurs as antiperthite inclusions in the leucosome plagioclase.

Enderbites (samples 350, 350-3, and 350-4) are rocks with Opx + Pl + Kfs + Qz + Chl + Bt + Mag assemblage (Fig. 3*b*). The medium- and coarse-grained matrix of plagioclase–quartz composition hosts scarce clusters of orthopyroxene grains. The plagioclase grains often bear antiperthitic K-feldspar ingrowths. Some orthopyroxene grains have

Table 1. Chemical composition of representative rocks of the Larba block (wt.%)

Sample	Rock group	SiO_2	TiO_2	Al_2O_3	$Fe_2O_{3\,tot}$	MnO	MgO	CaO	Na_2O	K_2O	P_2O_5	LOI	Total
348	Metapelite	53.90	1.22	18.60	13.10	0.18	6.28	2.38	2.11	1.83	B.d.l.	0.16	99.8
348-1	Metapelite	53.80	0.60	17.50	15.60	0.26	6.46	1.36	0.97	2.49	B.d.l.	0.90	99.9
348-4	Metapelite	65.60	0.59	18.50	5.60	0.04	3.09	1.12	1.33	3.38	B.d.l.	0.64	100.0
348-5	Metapelite	71.90	0.48	13.40	5.91	0.11	2.56	2.68	1.80	0.65	B.d.l.	0.42	99.9
359	Metapelite	65.80	0.65	15.80	8.26	0.09	3.25	1.97	1.84	2.16	B.d.l.	b.d.l.	99.9
359-5	Metapelite	60.90	0.62	18.20	8.25	0.10	3.66	1.83	2.03	2.88	B.d.l.	1.34	99.8
360	Metapelite	65.60	0.56	16.10	7.76	0.10	2.90	2.17	1.95	2.38	B.d.l.	0.38	99.9
360-1	Metapelite	66.80	0.62	16.10	6.47	0.07	2.57	1.60	1.98	3.49	B.d.l.	0.24	100.0
361	Metapelite	55.70	0.70	24.20	4.39	0.03	2.40	1.65	2.59	6.66	0.07	0.98	99.3
PT32-1	Metapelite	68.10	0.65	14.70	7.12	0.09	2.95	1.92	2.42	1.41	0.12	0.39	99.9
PT32-2	Metapelite	66.80	0.57	15.30	7.56	0.09	3.01	1.58	2.39	2.12	0.12	0.31	99.9
PT32-3	Metapelite	66.20	0.62	16.10	7.21	0.09	2.73	1.60	2.41	2.46	0.13	0.30	99.9
PT32-4	Metapelite	71.40	0.26	15.10	3.29	0.05	1.50	1.13	1.93	4.56	0.13	0.49	99.9
PT32-5	Metapelite	71.10	0.24	14.70	2.62	0.03	1.02	1.04	1.95	6.53	0.15	0.47	99.9
PT35-10-2	Metapelite	55.80	0.91	19.10	11.30	0.18	4.66	3.22	2.84	1.54	0.13	0.20	99.9
348-8	Metapelite	50.80	0.91	23.60	10.20	0.16	4.74	1.26	1.81	4.84	b.d.l.	1.24	99.6
350	Enderbite	69.30	0.15	16.80	2.36	0.02	1.12	3.97	4.73	0.87	0.08	0.59	100.0
350-3	Enderbite	67.10	0.36	17.40	3.24	0.04	1.54	4.36	4.63	0.99	0.11	0.16	99.9
350-4	Enderbite	58.20	1.27	22.20	4.72	0.03	0.81	5.32	5.31	1.56	0.25	0.30	99.9
350-1	Metabasite of group I	48.00	0.90	8.36	15.2	0.23	14.4	11.1	1.00	0.21	0.13	0.61	100.0
350-2	Metabasite of group I	46.10	1.47	15.00	14.9	0.21	8.75	10.7	2.41	0.34	0.09	0.17	100.0
362	Metabasite of group II	51.30	1.38	16.20	16.4	0.34	4.63	9.08	0.49	0.11	0.47	B.d.l.	100.0
364	Metabasite of group II	51.40	1.29	14.60	17.9	0.44	5.56	8.64	0.18	0.10	0.12	B.d.l.	99.7

Note. B.d.l. – below the detection limit.

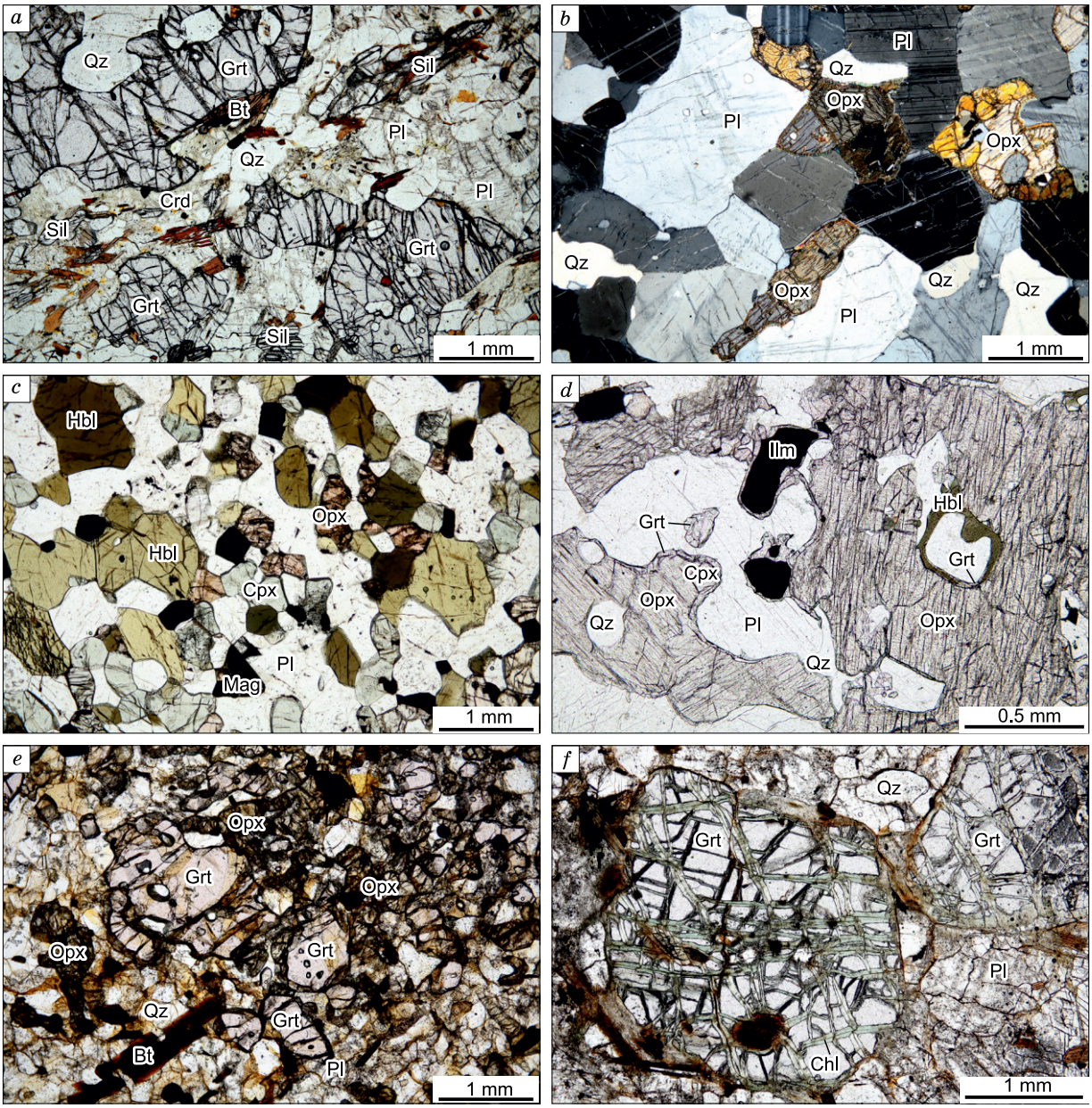

Fig. 3. Photomicrographs of the thin sections of the Larba block rocks. *a* – Metapelite (sample 348-4, Grt–Bt–Sil–Pl–Kfs–Qz–Crd–Pyh–Rt), *b* – enderbite (sample 350, Pl–Qz–Opx–Cpx–Kfs–Chl–Mag, with an analyzer), *c* – group I metabasites (sample 350-2, Hbl–Cpx–Opx–Pl–Mag), *d* – group II metabasites (sample 364, Grt–Opx–Cpx–Hbl–Pl–Kfs–Qz–Ilm), *e* – garnet–orthopyroxene–biotite gneiss (sample 359-2, Grt–Opx–Bt–Pl–Kfs–Qz–Ilm), *f* – replacement of garnet by chlorite in diaphthoric metapelite (sample 359-7, Grt–Bt–Chl–Pl–Qz–Rt). Parenthesized are the total assemblages.

clinopyroxene and K-feldspar rims (Fig. 4*b*) and later formed thin rims of pale green chlorite and, more seldom, amphibole. At the contact with orthopyroxene, they are sometimes enriched in fine inclusions of ore mineral.

Metabasites were divided into two groups according to their mineral and chemical compositions. Metabasites of group I (samples 350-1 and 350-2) are fine-grained rocks with an equigranular granoblastic texture, which correspond in chemical composition to gabbronorites and contain Opx + Cpx + Hbl + Pl + Mag assemblage (Fig. 3*c*). Metabasites of group II (samples 362 and 364) correspond in chemical composition to ferrogabbronorite. These are inequigranular rocks with Opx + Cpx + Hbl + Grt + Pl + Qz + Ilm + Cal assemblage, in which early Cpx–Opx–Hbl–Pl–Ilm paragenesis is variably replaced by later Grt–Opx–Pl–Qz paragenesis. Garnet occurs as large isometric crystals or irregular-shaped grains at more leucocratic and quartz-enriched sites of the rock and as fine crystals in plagioclase grains and thin rims over aggregates of pyroxene, ilmenite, and dark green hornblende at more melanocratic sites (Fig. 3*d*).

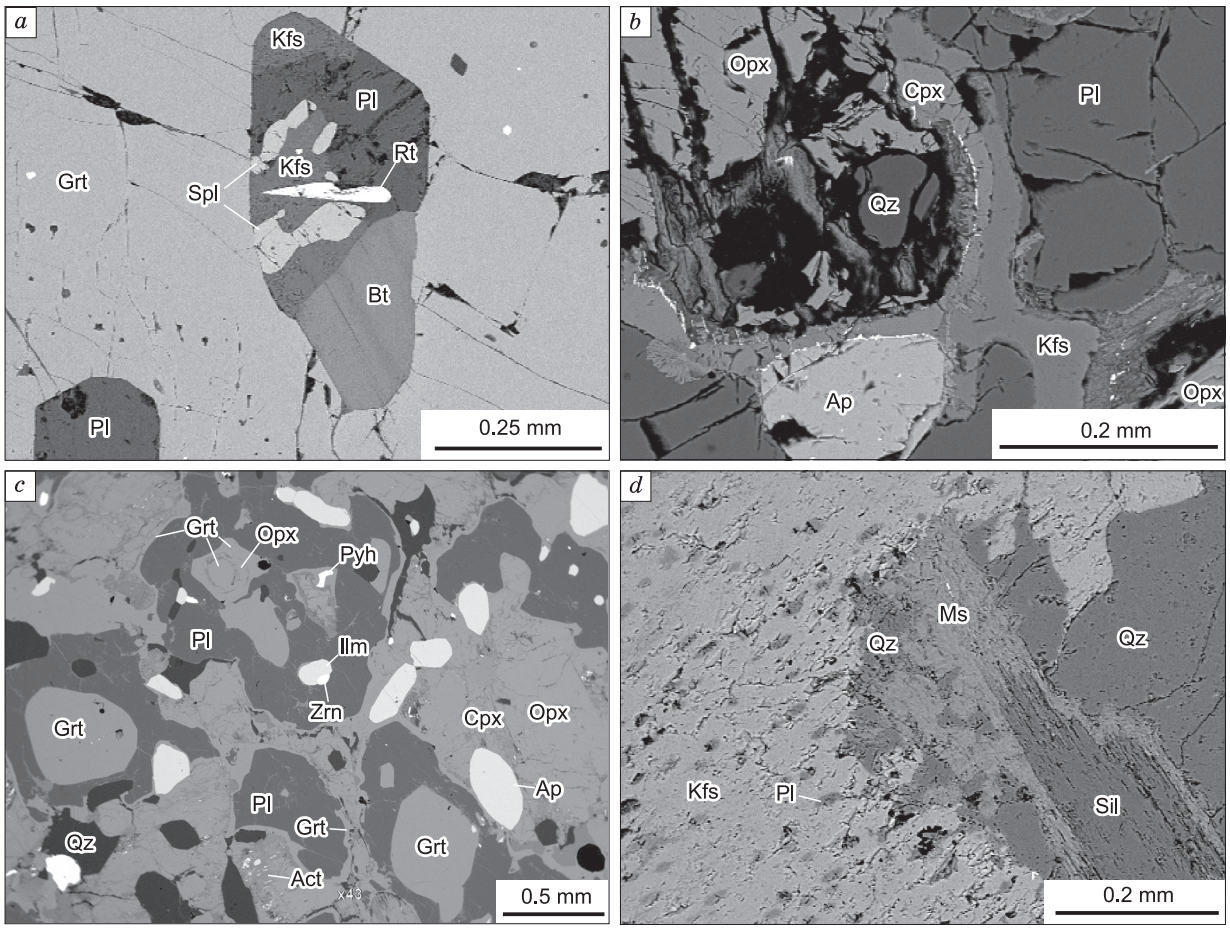

Fig. 4. Mineral relationships in the Larba block rocks (BSE images). *a* – Polymineral inclusion in garnet porphyroblast from metapelite (sample 359); *b* – clinopyroxene and K-feldspar rim over orthopyroxene and quartz grains in enderbite (sample 350); *c* – generations of garnet in group II metabasites (sample 362), *d* – development of muscovite with quartz over early sillimanite–K-feldspar paragenesis (sample PT32-4).

Locally, two generations of garnet are observed: fine garnet grains with thin orthopyroxene rims and garnet rims over this orthopyroxene (Fig. 4*c*). In addition, there are signs of the replacement of clinopyroxene by orthopyroxene. The latest alteration is the formation of pale green amphibole in the cleavage cracks of pyroxene.

PECULIARITIES OF ROCK-FORMING MINERALS

Garnets in the metapelites are of the Prp–Alm series, with a Grs impurity (Fig. 5*a*). Their grains show a weak zoning: The content of Alm increases and the contents of Grs and Prp decrease toward the edge. A Sps component is either absent or is negligible. The garnet grains with chlorite and mica in large cracks or in the rim are characterized by a drastic decrease in Prp content to ca. 30% and an increase in Alm content to 65% (Fig. 5*b*).

The garnets from orthopyroxene–biotite–granite gneiss also show a reverse zoning (Fig. 5*c*). They contain more Grs and less Prp than the garnets from metapelites ($Alm_{59–65}$ $Prp_{23–29}Grs_{8–10}Sps_{1–2}$).

In the group II metabasites, all garnet generations are similar in composition. They are predominantly Alm–Grs (Fig. 5*d*) with subordinate Prp and Sps (and significant contents of Adr). Their grains also have a reverse zoning: The content of Prp decreases and the content of Grs increases toward the edge.

Biotites in the metapelites are brown. Their grains with a sagenite lattice are found both in the rock matrix and in inclusions in garnet; they are often chloritized and spatially associated with garnet. There are also individual biotite grains associated with feldspar in the rock matrix.

Biotites differ significantly in composition, which is best seen on comparison of different groups of rocks (Suppl. Mat., Table ESM_1). The observed variations in Fe# and TiO_2 contents testify to incomplete equilibrium in the thin section, which is probably due to different degrees of regressive changes. For example, the biotite flakes in the inclusions in garnet are characterized by lower Fe# values than the biotite from the rock matrix. In general, the metapelite biotites contain 2.5–7.0 wt.% TiO_2, but the grains replacing garnet are poorer in it, TiO_2 = 0–4 wt.%. The biotites from

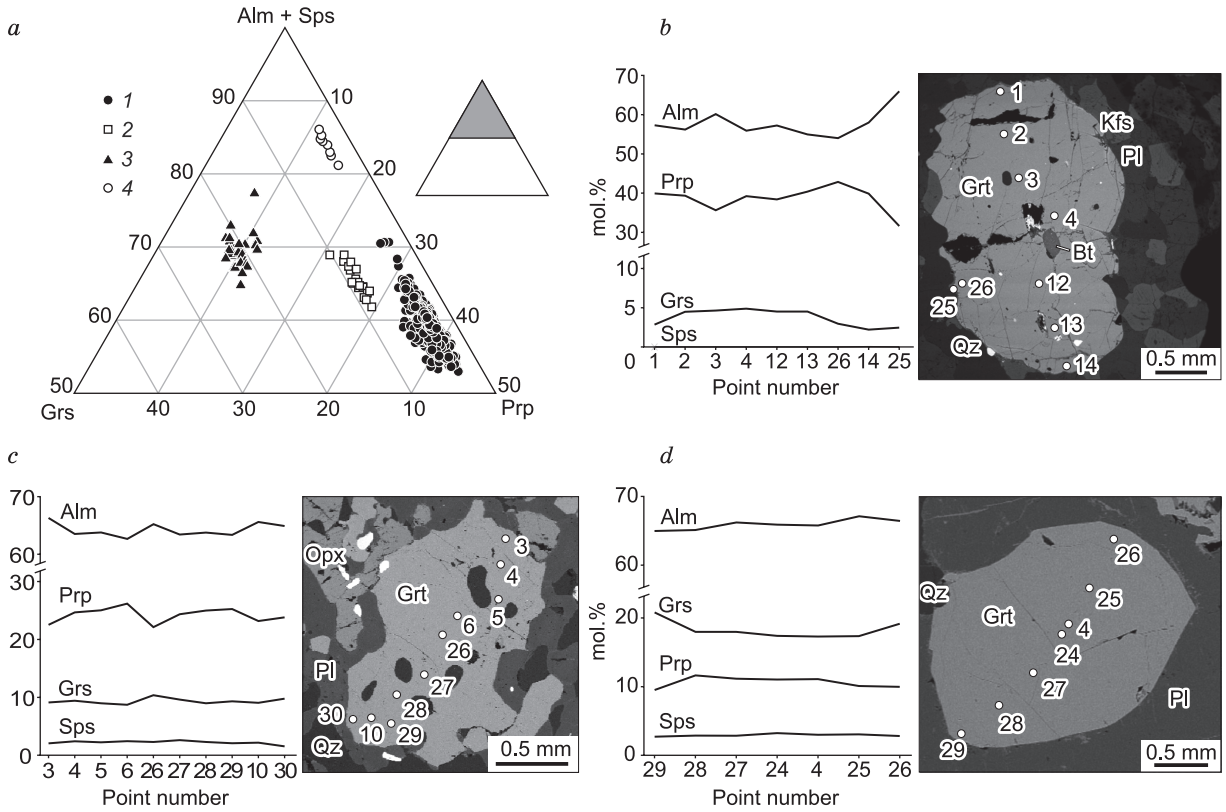

Fig. 5. Composition of garnets from the Larba block rocks: *a* – Grs–(Alm + Sps)–Prp diagram: *1* – metapelites, *2* – orthopyroxene–biotite–garnet gneiss, *3* – group II metabasites, *4* – garnet relics in diaphthoric metapelite; *b–d* – grain zoning profiles: *b* – metapelite (sample PT32-3), *c* – orthopyroxene–biotite–garnet gneiss (sample 359-2), *d* – group II metabasite (sample 362).

zones of intense diaphthoresis are characterized by higher Fe# values, 0.2–0.5 (in addition, they are often chloritized).

The biotites from enderbites and orthopyroxene–biotite–garnet gneiss show high contents of TiO_2 (3–5 and 5.5–6.3 wt.%, respectively) and elevated Fe# values (0.35–0.44 and 0.41–0.51). In the enderbites, the mineral is present mostly in assemblage with chlorite and replaces orthopyroxene.

Cordierite in the metapelites is highly magnesian (Mg# = 0.79–0.93), mostly pinitized.

Pyroxenes. Ortho- and clinopyroxenes in the metapelites have significantly varying compositions, although their variation intervals are narrow within the rock groups (Fig. 6; Suppl. Mat., Table ESM_1). In most rocks, orthopyroxenes correspond in composition to enstatite with Mg# = 0.49–0.55 in the orthopyroxene–biotite–garnet gneiss and with Mg# = 0.57–0.62 in the enderbite and group I metabasites. They also differ in Al_2O_3 content: It is high in orthopyroxene from the orthopyroxene–biotite–garnet gneiss (1.78–2.73 wt.%), lower in the group I metabasites (1.2–1.4 wt.%), and minor in the enderbite (0.18–0.72 wt.%). Orthopyroxene from the group II metabasites is ferrosilite with Mg# = 0.35–0.44 and Al_2O_3 = 0.04–0.54 wt.%. The lowest alumina content is observed in orthopyroxene growing over garnet.

Clinopyroxene in the studied rocks is represented by diopside with different Mg# values and Al_2O_3 contents: In the enderbites, it shows Mg# = 0.75–0.78 and Al_2O_3 = 0.68–1.14 wt.%; in the group I metabasites, Mg# = 0.69–0.76 and Al_2O_3 = 2.46–2.86 wt.%; and in the group II metabasites, Mg# = 0.52–0.60 and Al_2O_3 = 0.26–1.33 wt.%. The clinopyroxenes contain a Na_2O impurity; its maximum content is found in the group I metabasites, 0.34–0.56 wt.%. In the group II metabasites, clinopyroxene is observed mainly as relict grains inside large orthopyroxene porphyroblasts.

Amphiboles in the group I metabasites are texturally in equilibrium with pyroxenes and are pargasite hornblende (Suppl. Mat., Table ESM_1). The group II metabasites bear amphiboles of two varieties. Scarce grains of dark green hornblende corresponding in composition to potassic chlorhastingsite (ca. 50%) occur in intimate assemblage with orthopyroxene and garnet (but are also overgrown with thin garnet rims). Some hornblende grains show variations in composition toward the edges: The Mg# value decreases from 0.53–0.56 to 0.47–0.53, the TiO_2 content decreases from 2.01–2.64 to 1.09–2.14 wt.%, and the Cl content increases from 0.78–0.94 up to 1.03–1.39 wt.%. Secondary amphibole, corresponding in composition to actinolite and ferroactinolite, is developed along the cleavage cracks of orthopyroxene.

Feldspars. Plagioclase in the metapelites corresponds in composition to oligoclase–andesine (Suppl. Mat., Table ESM_1). There is also a group of plagioclases in the inclusions in garnet, which have a higher content of anorthite

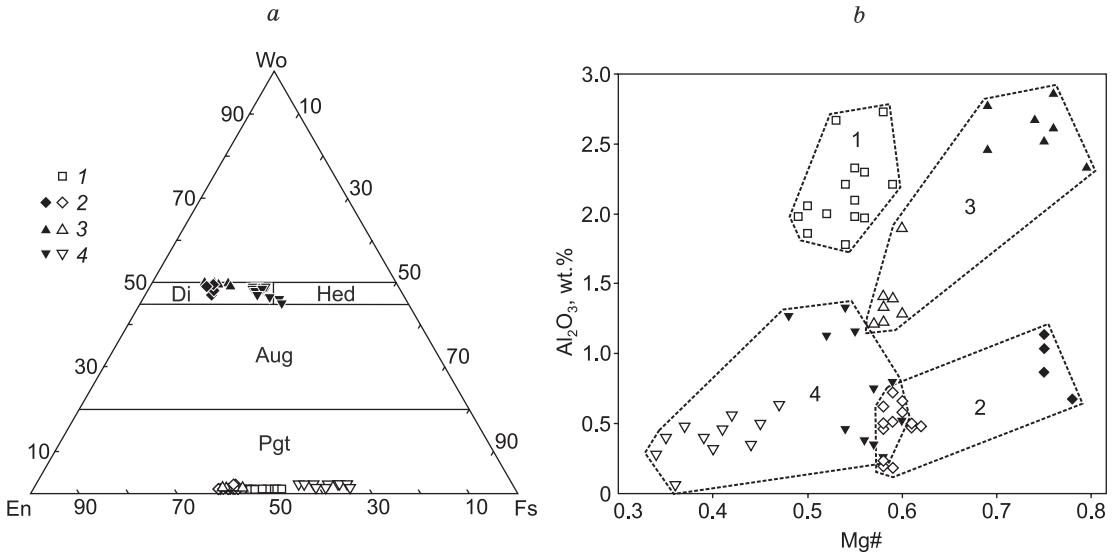

Fig. 6. Compositions of pyroxenes from the Larba block rocks: *a* –En–Wo–Fs diagram; *b* – Al_2O_3–Mg# diagram. White symbols mark orthopyroxenes, and black symbols mark clinopyroxenes. *1* – orthopyroxene–biotite–garnet gneiss; *2* – enderbite; *3* – group I metabasites; *4* – group II metabasites.

component than the plagioclase in the matrix. In the rock samples subjected to low-temperature metamorphism, plagioclase is often saussuritized and occurs as perthites in K-feldspar, corresponding in composition to albite.

Plagioclase in the enderbite contains antiperthites and corresponds in composition to oligoclase–andesine with 29–35% An.

Plagioclase in the group I metabasites corresponds in composition to andesine $An_{47–50}$. One plagioclase grain has composition An_{84}; it is present as a rounded inclusion in andesine at the contact with an altered rim over the amphibole grain. Plagioclase in the group II metabasites is separated from dark-colored minerals by a garnet or quartz rim and compositionally corresponds to bytownite–anorthite $An_{86–94}$.

K-feldspar in the metapelites contains numerous perthites. In the enderbite, it occurs both in antiperthites and in the reaction rim over orthopyroxene grains. The K-feldspar grains are virtually of the same composition; they are represented by orthoclase with an Ab impurity (up to 15%).

RESULTS OF ROCK THERMOBAROMETRY

Metapelites (aluminous gneisses). For most samples, calculations were made for the Grt + Bt + Sil + Pl + Qz paragenesis with three possible linearly independent reactions, which permits estimating the degree of nonequilibrium of the chosen mineral compositions. Sometimes, the above paragenesis additionally included cordierite, ilmenite, and rutile increasing the number of linearly independent reactions to six. This led to significantly worse line convergence, which is to be expected as the number of linearly independent reactions increases. However, this indicates nonequilibrium between the cordierite and the earlier formed paragenesis. At the same time, when cordierite is added, the pressures slightly decrease as compared with those in the absence of this mineral.

All tested samples show variations in mineral composition even within small sites, with the widest variations observed for biotites, which is reflected in the *P–T* diagrams as groups of points arranged along the pressure axis and demonstrating similar degrees of MSD convergence (Fig. 7*a*). This is due to the fact that when the lines of thermometric reactions of the Grt–Bt equilibrium exchange and the reaction 3Alm + 3Eas + 4bQtz = 2Prp + 3Ann + 4Sil are consistent, most of other lines are confined to the intersection of these two with the line of the third linearly independent reaction, the Grt–Sil–Pl–Qz barometer. Wide pressure intervals for each group of points are mostly due to the slight variations in Grs content in garnet, when they are low (3–4 mol.%) and thus increase the influence of analytical errors, whereas the fluctuations in An content in plagioclase play a smaller role.

The most magnesian compositions of biotites, mainly in the inclusions in garnet porphyroblasts, form low-temperature groups, whereas more ferruginous biotites near these porphyroblasts in the rock matrix form high-temperature groups. The lowest pressures are specific to the plagioclase inclusions in garnet (with high An contents), and the highest pressures, to the grains in the matrix (with high Ab contents). The bimodal distribution of *P–T* parameters, including those with good convergence of the equilibrium lines (Fig. 7*a*), is typical of many aluminous-gneiss samples. Most likely, it reflects stepwise granulite metamorphism: lower-temperature and low-pressure conditions at the progressive stage, established from the inclusions in garnet porphyroblasts during the growth of the latter, and conditions at the peak stage (and similar conditions at the progressive or

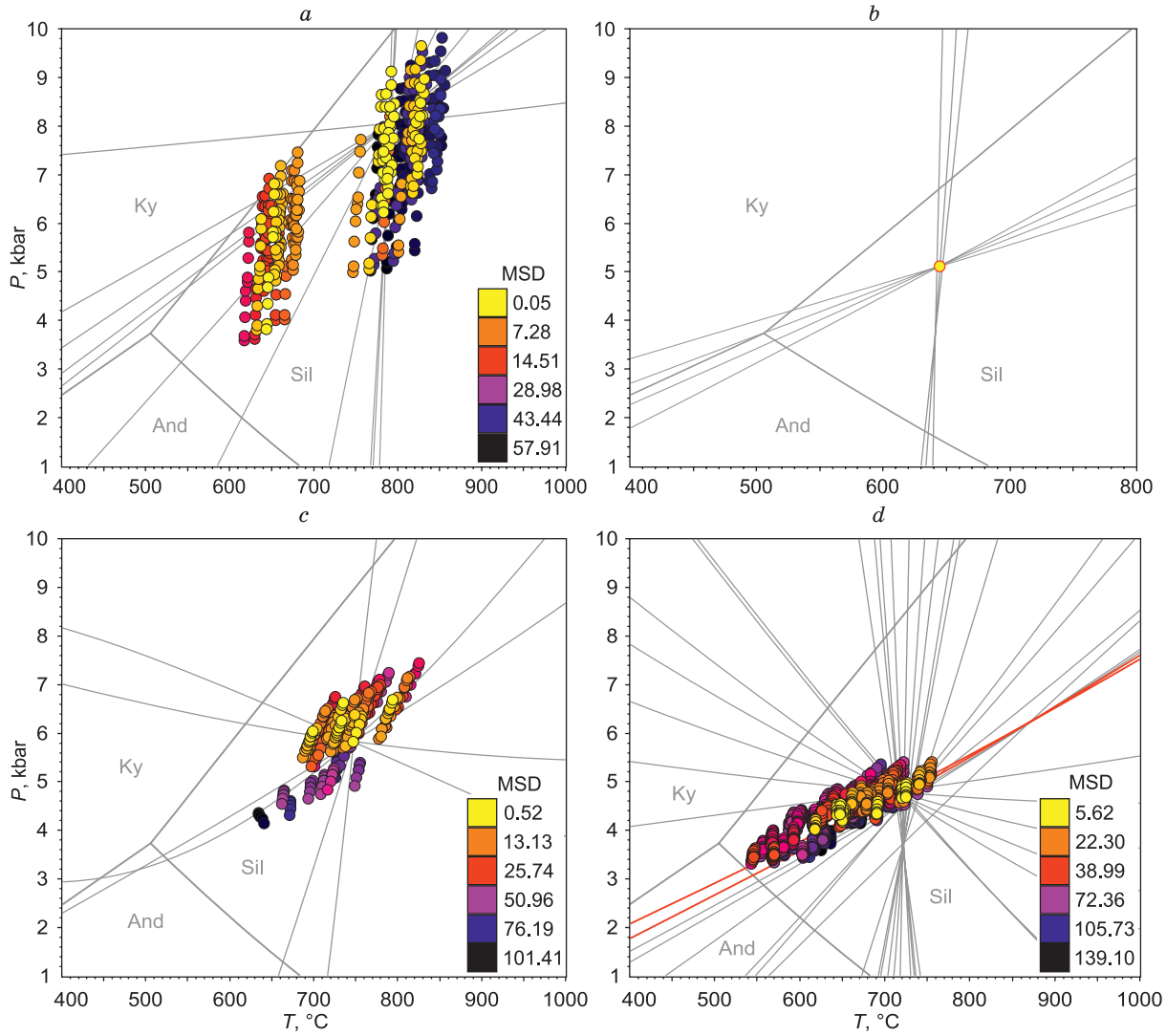

Fig. 7. Representative *P–T* diagrams for some samples, constructed using the winTWQ v.2.64f software with the DEC06 (Berman, 2007) (*a*, *c*, *d*) and BA96A (Berman and Aranovich, 1996) (*b*) databases and the TWQ_Comb and TWQ_View software (Dolivo-Dobrovolsky, 2006*a*, *b*). Points for all possible combinations limit the maximum domain of uncertainty; the points with minimum MSD values mark the domains of the most probable values (these are the domains from which combinations of analytical data meeting the required structural relationships in electron microscope images were then chosen). The best converged reaction lines for combinations of mineral compositions and the reference reaction lines for polymorphic Al_2SiO_5 transitions are also shown.
a – Aluminous gneiss (sample PT32-4, local site 1 of transparent polished plate); *b* – SiO_2-undersaturated polymineral Bt–Pl–Sil–Spl inclusion in garnet from aluminous gneiss (sample 359, local site 6); *c* – Grt–Opx–Pl–Qz paragenesis of orthopyroxene–biotite–garnet gneiss (sample 359-2, local site 3); *d* – Grt–Opx–Cpx–Pl–Qz paragenesis of group II metabasite (sample 362). Lines of the reactions Grs + 2Fs + βQz = 2Hd + An and Alm + 2Grs + 3βQz = 3Hd + 3An corresponding to the reaction structures in the thin sections of rocks are shown (these reactions shift to the left with decreasing temperature and/or increasing pressure).

regressive steps), determined from the edges of porphyroblasts and from the minerals of the rock matrix.

It is worth dwelling on the calculation of *P–T* parameters for the SiO_2-undersaturated polymineral Bt–Pl–Sil–Spl–Rt inclusion in the garnet from aluminous gneiss (sample 359, local site 6). For this purpose, we used the thermodynamic database BA96A (Berman and Aranovich, 1996) including a better description of the aluminum spinel solid solution. Diagrams with perfect convergence of three linearly independent reactions were constructed for it under conditions of amphibolite facies metamorphism: $T = 645$ °C, $P = 5.2$ kbar (Fig. 7*b*). Most likely, the paragenesis of the inclusion formed during the growth of a garnet porphyroblast replacing biotite with small staurolite grain at the early, progressive stage of granulite metamorphism. This might be indicated by the high contents of Zn in spinel (Suppl. Mat., Table ESM_1), because staurolite is the main concentrator of zinc in metapelites under conditions of amphibolite facies metamorphism. Apparently, the spinel grew at the site of rock that was already protected from the inflow of a silica-rich fluid from the quartz-containing matrix. K-feldspar and rutile grains associated with the spinel suggest Ti-containing biotite as one of

the reagents, in addition to staurolite. This process (ignoring Ti) can be described by the balanced dehydration reaction $31Bt + 9St = 31Kfs + 24Grt + 57Hrc + 40H_2O$.

Orthopyroxene–biotite–garnet gneiss. The rock (sample 359-2) consists of two components: mostly quartz-free orthopyroxene–plagioclase and quartz- and garnet-enriched as a result of migmatization. Calculations were made for the Grt–Opx–Pl–Qz paragenesis from a wide transition zone where all these minerals coexist, not reacting with each other. Biotite here occurs as scarce single grains of unclear genesis. Its addition to the system leads to a strong degradation of the convergence of the lines; thus, the resulted system demonstrates three linearly independent reactions. The compositions of minerals from the two examined local sites of the thin section show similar *P–T* parameters corresponding to the transition zone between the granulite facies of moderate-pressure metamorphism and the amphibolite facies (Fig. 7*c*).

Metabasites. The rock corresponding in chemical composition to ferrogabbronorite contains Grt–Opx–Cpx–Amp–Pl–Qz–Ilm–Cal paragenesis (samples 362 and 364). Garnet forms at least two generations: The early one is represented by isometric crystals and irregularly shaped grains in the plagioclase mass (these grains are associated with quartz segregations), and the late generation forms thin rims over other ferromagnesian minerals (and over garnet grains with orthopyroxene rims). The compositions of garnets of both generations are nearly the same. Orthopyroxene crystallized in stages: Some of its grains formed after the garnet of early generation (they are characterized by ultralow contents of Al_2O_3). Clinopyroxene is observed as relict grains, usually inside larger orthopyroxene porphyroblasts. Amphiboles are of two varieties: an early one, texturally in equilibrium with late orthopyroxene, with high contents of potassic chlorhastingsite (ca. 50%), and a late one, present mainly in the cleavage cracks of orthopyroxene and corresponding in composition to ferroactinolites.

The thermodynamic properties of potassic chlorhastingsite are unknown; therefore, amphiboles were excluded from the system. Calculations for the Grt–Opx–Cpx–Pl–Qz paragenesis characterized by four linearly independent reactions (with ignored Al–Opx, whose content is negligible in the orthopyroxenes) show that the compositions of all minerals are close to the equilibrium ones at low pressures and temperatures (Fig. 7*d*), which is unusual for rocks with this mineral composition.

To elucidate the conditions of formation of the Grt–Opx–Cpx–Pl–Qz paragenesis, we constructed phase diagrams (pseudosections) for a rock of given composition with different H_2O contents. Calculations were made using the GeoPS software (Xiang and Connolly, 2022) with the thermodynamic database DS622 from the THERMOCALC complex and the same models of solid solutions and melt as in the research by Green et al. (2016), which is concerned with thermodynamic modeling for rocks of this composition series. We have established that the Grt–Opx–Cpx–Pl–Qz paragenesis is stable at these *P–T* parameters under water deficiency (≤1.5 mol.%) or at low water activity (Fig. 8). The latter is possible both with a high-CO_2 fluid (which is

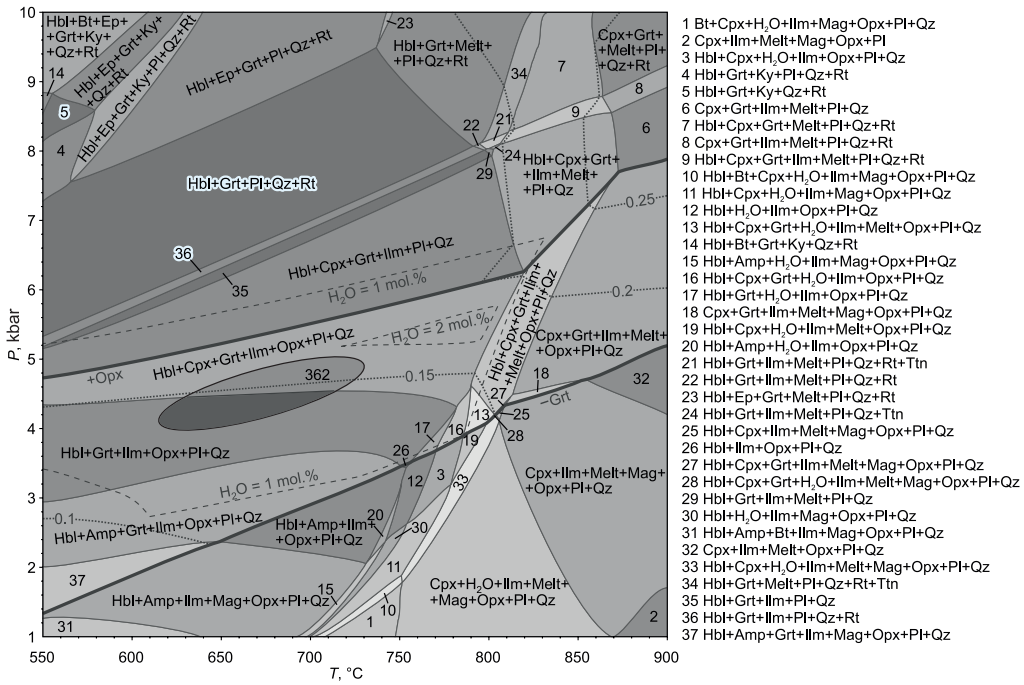

Fig. 8. Phase diagram (pseudosection) constructed for the group II metabasite (sample 362) with H_2O = 1.5 mol.% using the GeoPS software (Xiang and Connolly, 2022), the DS622 thermodynamic database, and the solution models borrowed from Green et al. (2016). The results of geothermobarometric calculations using the TWQ program with the DEC06 database (ellipse) fall in the low-temperature field of the Hbl–Cpx–Grt–Ilm–Opx–Pl–Qz paragenesis. Dashed line shows the boundaries of this field with two other water contents in the system. Dotted line marks the Mg# isopleths in garnet, and thick lines show the boundaries of the fields of orthopyroxene-containing and garnet-free parageneses. Oxides (mol.%): SiO_2 = 54.95, TiO_2 = 1.11, Al_2O_3 = 10.23, FeO = 13.19, MnO = 0.31, MgO = 7.39, CaO = 10.42, Na_2O = 0.51, K_2O = 0.08, H_2O = 1.5, O_2 = 0.32.

evidenced by the presence of calcite in the rock) and with a salt-enriched fluid (which is evidenced by high Cl contents in the amphibole of early generation). As the H_2O content increases, pyroxenes must be completely replaced by amphiboles. Note that the modal contents of garnet and quartz here increase (and those of pyroxenes decrease) with increasing pressure and/or decreasing temperature, which corresponds to the reactions observed in the thin sections. At the same time, this pseudosection gives an insight into the parageneses that would exist under moderate- and high-pressure granulite facies conditions: Orthopyroxene appears only at pressures below 8 kbar, whereas garnet with Mg# ≈ 0.25 should be present at pressures above 4.5–5.0 kbar. The samples, however, lack an early (granulite) garnet: All its generations are superposed and show minor compositional variations, which indicates that the early paragenesis of the group II metabasites formed at a pressure of <5 kbar and did not experience granulite metamorphism that put imprints on the metapelites and orthopyroxene–garnet–biotite gneisses. As follows from the $Mg\#^{Grt}$ isopleths, the Mg# values of garnet under equilibrium conditions (i.e., in a completely recrystallized rock) should be slightly higher than the values measured in the sample (ca. 0.1), which correspond to still lower *P–T* parameters.

Judging by the mineral assemblages, the lowest-temperature changes in the rocks correspond to the conditions of the chlorite–muscovite subfacies of the greenschist facies. The degree of metamorphism at this stage was not evaluated by multi-equilibrium thermobarometry because of the insufficient number of minerals in the latest parageneses of rocks that underwent diaphthoresis and because of the high degree of their nonequilibrium.

U–Th–Pb ISOTOPE STUDIES OF ENDERBITES

U-Th-Pb isotope studies (SHRIMP-II, Karpinsky All-Russian Research Geological Institute, St. Petersburg) were carried out for 17 zircon grains from the enderbite samples (sample 350, Table 2).

Zircon is present as pink and colorless subhedral crystals 100–300 μm in size (Fig. 9). Approximately half of the crys-

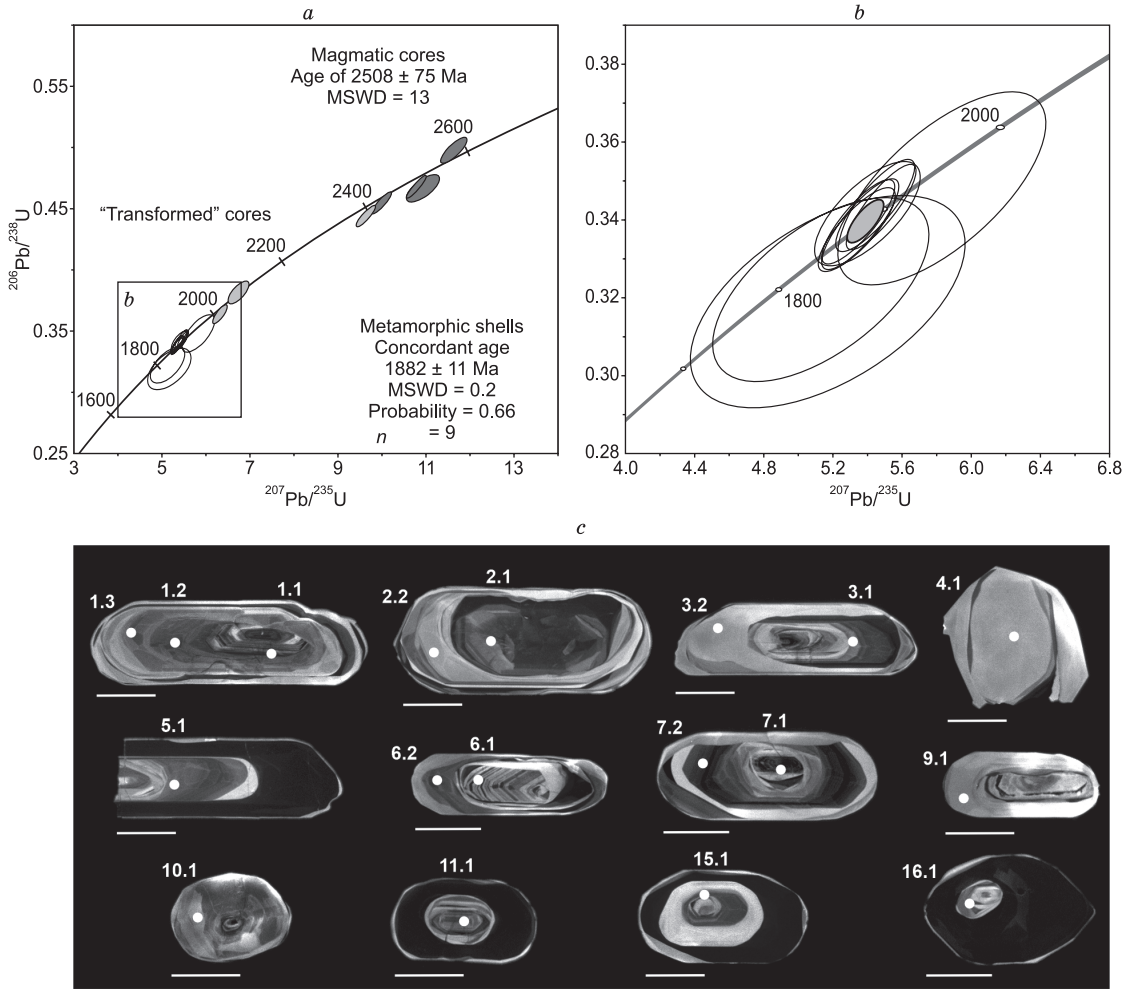

Fig. 9. Concordia diagrams for zircon from the Larba block enderbites: *a* – with the isotope composition points of all analyzed zircon grains; *b* – fragment of the diagram with results for the metamorphic shells of the grains; *c* – CL images of the analyzed zircon grains with sampling points (scale bar of 0.1 mm).

Table 2. Results of U–Pb dating of enderbites from the Larba block

Spot	$^{206}Pb_c$, %	U ppm	Th ppm	$^{232}Th/^{238}U$	$^{206}Pb^*$, ppm	$^{206}Pb/^{238}U$, age		$^{207}Pb/^{206}Pb$, age		D, %	$^{238}U/^{206}Pb$	%	$^{207}Pb/^{206}Pb$	%	$^{238}U/^{206}Pb^*$	%	$^{207}Pb^*/^{206}Pb^*$	%	$^{207}Pb^*/^{235}U$	%	$^{206}Pb^*/^{238}U$	%	Error corr.
14.1	0.00	129	58	0.46	37.50	1875	22	1875	17	0	2.963	1.3	0.1147	0.96	2.963	1.3	0.1147	0.96	5.338	1.7	0.3375	1.3	0.813
6.2	0.00	153	79	0.53	44.70	1884	22	1868	16	–1	2.946	1.3	0.1142	0.89	2.946	1.3	0.1142	0.89	5.347	1.6	0.3395	1.3	0.829
2.2	0.00	43	28	0.69	12.50	1894	27	1874	30	–1	2.927	1.6	0.1146	1.7	2.927	1.6	0.1146	1.7	5.4	2.3	0.3416	1.6	0.706
5.1	0.00	139	60	0.45	40.40	1881	23	1875	17	0	2.951	1.4	0.1147	0.93	2.951	1.4	0.1147	0.93	5.358	1.7	0.3389	1.4	0.831
7.2	0.00	177	82	0.48	52.20	1902	21	1892	15	–1	2.913	1.3	0.11576	0.81	2.913	1.3	0.11576	0.81	5.479	1.5	0.3433	1.3	0.847
13.2	0.00	137	62	0.47	40.60	1905	23	1878	17	–1	2.909	1.4	0.1149	0.93	2.909	1.4	0.1149	0.93	5.445	1.7	0.3437	1.4	0.830
4.1	0.00	11	1	0.05	3.29	1925	48	1979	56	3	2.873	2.9	0.1215	3.1	2.873	2.9	0.1215	3.1	5.83	4.2	0.3481	2.9	0.676
10.1	0.19	51	46	0.95	20.40	2472	32	2555	27	3	2.136	1.6	0.1714	1.5	2.14	1.6	0.1697	1.6	10.93	2.3	0.4673	1.6	0.692
1.2	0.18	94	74	0.81	40.20	2607	30	2550	17	–2	2.003	1.4	0.1708	0.96	2.007	1.4	0.1692	1	11.63	1.7	0.4984	1.4	0.802
12.1	0.09	44	49	1.15	20.50	2778	39	2651	19	–5	1.855	1.7	0.1806	1.1	1.857	1.7	0.1798	1.1	13.36	2.1	0.5386	1.7	0.839
7.1	0.17	122	36	0.30	38.30	2004	23	2039	18	2	2.738	1.4	0.1273	0.92	2.743	1.4	0.1258	1	6.32	1.7	0.3646	1.4	0.797
15.1	0.43	58	29	0.52	19.00	2087	29	2069	29	–1	2.604	1.6	0.1317	1.3	2.616	1.6	0.1279	1.6	6.74	2.3	0.3823	1.6	0.704
2.1	0.15	202	34	0.17	74.40	2292	24	2414	15	5	2.339	1.3	0.1574	0.87	2.342	1.3	0.1561	0.91	9.19	1.6	0.4269	1.3	0.814
1.1	0.11	148	33	0.23	56.50	2371	26	2426	12	2	2.247	1.3	0.1581	0.68	2.25	1.3	0.1572	0.73	9.63	1.5	0.4445	1.3	0.875
16.1	0.09	136	51	0.39	53.30	2418	27	2446	12	1	2.195	1.3	0.1599	0.69	2.197	1.3	0.1591	0.72	9.99	1.5	0.4552	1.3	0.877
13.1	0.17	98	24	0.26	38.50	2419	29	2515	19	4	2.192	1.5	0.1672	1.1	2.196	1.5	0.1657	1.2	10.4	1.9	0.4553	1.5	0.782
11.1	0.10	235	18	0.08	94.70	2477	26	2527	9	2	2.132	1.3	0.16774	0.51	2.134	1.3	0.16689	0.54	10.78	1.4	0.4685	1.3	0.920
6.1	0.04	169	28	0.17	76.80	2732	29	2620	17	–4	1.894	1.3	0.1769	1	1.895	1.3	0.1765	1	12.84	1.7	0.5278	1.3	0.780

Note.* – Isotope ratios corrected for the blank sample and fractionation; D – discordance, Error corr. – correlation coefficient of the $^{207}Pb/^{235}U$ and $^{206}Pb/^{238}U$ errors.

tals are isometric, and the other are elongated, with the side ratio of 1:2–1:4. In the elongated crystals, the prism and bipyramid faces, usually smoothed, are clearly seen. All crystals have a complex structure, which is well seen in cathodoluminescence (CL) images. Most grains have several sequential "shells", often alternating from very light to very dark, which is correlated with their U contents: from 6–8 ppm in the light parts up to ca. 200 ppm in the darker ones. Some inner shells are locally overgrown with new ones (Fig. 9*c*, grain 7). The shells (except for a few ones) are nonuniform, which is well seen in the CL images (Fig. 9*c*). Some cores of the grains that crystallized from melt (Fig. 9*c*, grain 6) show an oscillatory zoning, which is typical of magmatic zircon. In most grains, however, the core zoning varies from noticeable irregular to diffuse. As shown by isotope analysis of the grain cores (which is discussed below), it is difficult to predict the age of individual shells only from their appearance, based on the assumption that some of them are the product of magma crystallization and the other are the product of at least partial recrystallization during metamorphism. The outer shell is uniform black, possibly with a high uranium content. There is a transition zone between the core and the shell (Fig. 9*c*, grains 7 and 15).

A total of 23 isotope measurements were made, including seven discordant. The measurement results (except for the inconsistent values) are given in Table 2. Zircon from enderbite is characterized by low contents of U (6–235 ppm), Pb (2–94 ppm), and Th (1–82 ppm). The Th/U ratio in both magmatic cores and metamorphic shells is within 0.05–0.95 (Table 2).

In the concordia diagram (Fig. 9*a*, *b*), the isotope composition points of the metamorphic shells form a compact cluster. The concordant $^{207}Pb/^{206}Pb$ age of the shells is 1882 ± 11 Ma. The measured isotope composition of the magmatic cores covers a wide age range along the concordia (2446 ± 12–2555 ± 27 Ma). An interesting example is grain 1, whose age, according to three measurements, becomes older in passing from the core to the edge (Fig. 9, Table 2). This indicates the specific domain structure of the zircon, as in other regions, which is briefly discussed below.

Thus, at a first approximation, the time of magmatic crystallization of enderbites is estimated at ca. 2.5 Ga; it is impossible to evaluate the age more precisely from the given zircon sample. The above estimate coincides with the earlier results of dating of the Larba enderbites (Moskovchenko et al., 1993). The time of the metamorphic stage of recrystallization of magmatic grains is estimated as 1882 ± 11 Ma. The error of the used SIMS dating of the metamorphic shell of zircon is smaller than 1% (±18 Ma for the obtained age (Williams, 1997)). The time of the latest superposed metamorphism that formed the black thin shells was not dated because of few local points of SHRIMP-II measurement.

THE Sm–Nd SYSTEM OF GRANULITES AND ENDERBITES

The model Nd age of the supracrustal metamorphic rocks of the Larba block, intruded by enderbites with an age of 2.51–2.54 Ga, was estimated at $T_{Nd}(DM)$ = 2.8–3.0 Ga

Table 3. Results of Sm–Nd analysis of rocks of the Larba block

Sample	Sm	Nd	$^{147}Sm/^{144}Nd$	$^{143}Nd/^{144}Nd$	Err	$e_{Nd}(0)$	$e_{Nd}(T)$	$T_{Nd}(DM)$
	ppm							
350, enderbite	1.430	10.13	0.0853	0.510876	4	–34.4	2.2	2.57
350-3, enderbite	1.556	10.31	0.0912	0.510970	9	–32.5	2.1	2.58
348-5, metapelite	4.297	28.46	0.0912	0.510681	4	–38.2	–0.1	2.95
362, metabasite	9.679	45.44	0.1288	0.511481	5	–22.6	1.9	2.81
LA-508*, metapelite	3.800	22.30	0.1027	0.510975	2	–32.4	1.5	2.84

* (Velikoslavinskii et al., 2017).

(Table 3). These data indicate that the protoliths of the metamorphic rocks are not older than 2.8–3.0 Ga, i.e., are not Paleoarchean, as was considered earlier (Glukhovskii and Sintserova, 1979), but, most likely, Mesoarchean. The model Nd age of the enderbites, $T_{Nd}(DM) \sim 2.6$ Ga, coincides, within the determination error, with the estimated age of their intrusion but differs significantly from the model Nd age of the host metamorphic rocks.

In the $\varepsilon_{Nd}(t)$–age diagram (Fig. 10), the composition points of the enderbites lie much higher than the Nd isotope evolution field of the supracrustal rocks of the Larba block. The Nd isotope composition of the enderbites differs from that of the depleted mantle by only two units. These data apparently point to the juvenile crustal source of the enderbites, possibly with a slight contamination of the enclosing rocks.

DISCUSSION

Position of enderbites and granulites of the Larba block on the general scale of the regional endogenous events. Analysis of the morphology and internal structure of zircon grains from the Larba enderbites apparently shows that only a few sites of the complex crystals have preserved their primary structure and, probably, composition. Note that this is typical of rocks that have undergone high-grade metamorphism; e.g., domains of different ages were identified in a single zircon crystal in rocks of the Lewisian Complex in Scotland (Friend and Kinny, 1995). There are also other examples of zircon grains with a complex structure, in which extremely small sites or domains ("nanospheres") with the uneven distribution of isotope elements were distinguished (Kusiak et al., 2015, 2019).

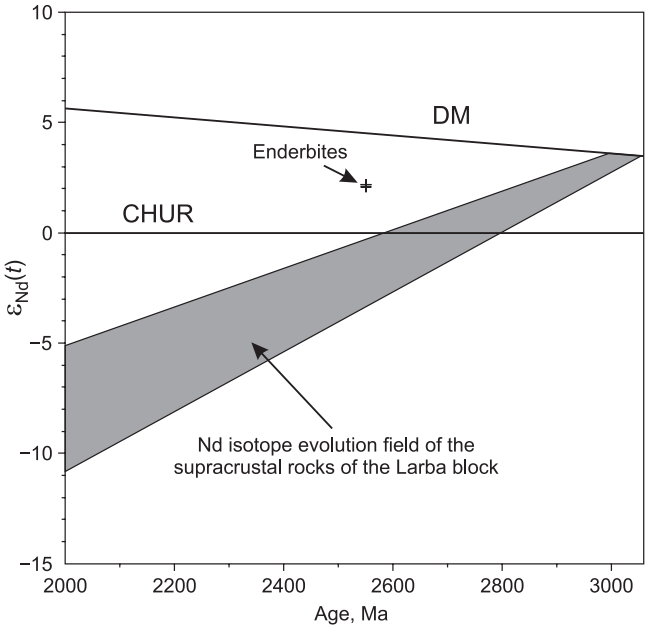

Fig. 10. $\varepsilon_{Nd}(t)$ – age diagram for enderbites and supracrustal rocks of the Larba block.

With regard to the big errors of age determination, the age of the Larba enderbites might coincide with the stage of postcollisional magmatism on the southern margin of the Siberian craton (Dzhugdzhur–Stanovoi superterrane and Stanovoi structural suture). Typical representatives of this magmatic stage are: Kalar charnockite–anorthosite complex in the Stanovoi suture zone, 2623 ± 23 Ma (Salnikova et al., 2004; Larin et al., 2006), the above-mentioned Khorogochi and Maristyi gabbroid massifs of the Ilikan unit, and anorthosite of the Dambuki block of the Dzhugdzhur–Stanovoi superterrane, 2643 ± 31 Ma (Buchko and Sorokin, 2010). All these igneous rocks formed in the period 2.67–2.60 Ga.

One of the magmatic events that might be responsible for the intrusion of the Larba enderbites is within-plate *A*-type granite magmatism in the zone of junction of the Chara–Olekma and Aldan blocks of the Aldan Shield, dated by the zircon U–Pb method at 2522 ± 2–2398 ± 4 Ma (Salnikova et al., 1997; Larin et al., 2012). However, this is only an age correlation, because the studied enderbites are not similar in the contents of major elements to *A*-type granites (Table 1). The age of synmetamorphic charnockites of the Altual Complex in the Stanovoi suture zone, 2627 ± 16 Ma (Larin et al., 2006), testifies to a nearly coeval or synchronous high-temperature metamorphism. Basic magmatism was earlier established in the Stanovoi Complex, based on the zircon U–Pb age of metagabbro with "within-plate" geochemical characteristics, 2653 ± 4 Ma (sample K-1516, data from S.D. Velikoslavinskii, Institute of Precambrian Geology and Geochronology RAS, St. Petersburg).

The time of crystallization of the studied enderbite was determined with a large error: 2508 ± 75 Ma (MSWD = 13) and 2546 ± 52 Ma (from the upper intercept of discordia and concordia). It is difficult to interpret this enderbite magma-

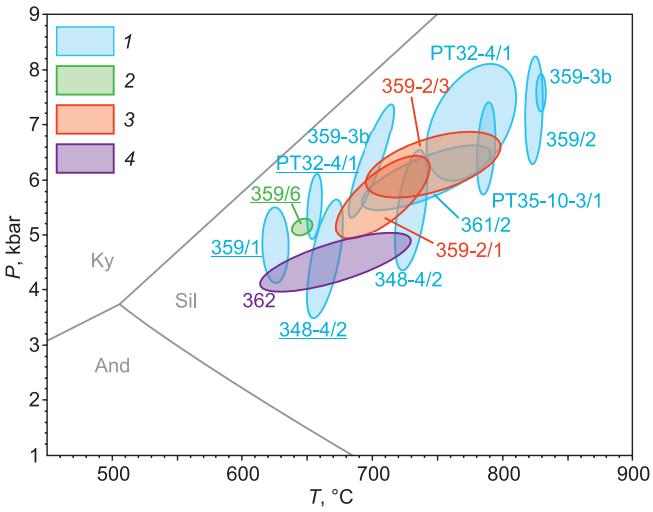

Fig. 11. Summary of *P–T* diagram with geothermobarometry results for all studied samples of the Larba block. *1* – Aluminous gneisses; *2* – spinel inclusion in garnet from aluminous gneiss; *3* – orthopyroxene–biotite–garnet gneiss; *4* – group II metabasites. Ellipses outline *P–T* domains with good convergence of the equilibrium lines for the marked samples. The sample numbers (labels of the domains) with *P–T* parameters determined from the inclusions in garnet porphyroblasts are underlined.

tism unambiguously, although the event dated at 2.4–2.5 Ga is widely manifested in ancient cratons, usually as basic magmatism and less often as bimodal magmatism. A typical result of such magmatism is a complex of layered basic intrusions on the Fennoscandian Shield (Glebovitskii, 2005).

Thus, judging by the composition of the studied enderbites (Table 1), these rocks are not products of within-plate magmatism. Taking the above data into account, we believe that enderbite magmatism, most likely, completed the late Archean collision–postcollisional stage, but this viewpoint calls for substantiation.

Geothermobarometry results. The geothermobarometry results for all rock samples are presented in the summary diagram (Fig. 11). They were obtained by choosing combinations of the rock compositions with satisfactory MSD values corresponding to certain textural characteristics (the closest arrangement of grains with measured compositions, separation of grains from inclusions and from the rock matrix, localization in different zones of porphyroblasts); therefore, the rock domains in the summary diagram are significantly smaller than those in Fig. 7 showing the points for all possible combinations and limiting the maximum domain of uncertainty. These domains might reflect, as a first approximation, the superposed determination errors related to the actual variations in mineral compositions and to the analytical errors and inaccuracies of thermodynamic models. The summary diagram shows a wide range of *P–T* parameters.

The established conjugate changes in pressure and temperature (Fig. 11) might reflect: (i) the *P–T* conditions at the progressive stage of granulite metamorphism, determined from the inclusions of metapelites in garnet porphyroblasts (most of the low-temperature domains in the diagram), (ii) the peak conditions, determined from the edges of porphyroblasts and the matrix minerals and corresponding to moderate-pressure granulite facies (7–8 kbar, 800–850 °C), and (iii) the regressive stage, at which orthopyroxene–biotite–garnet gneisses formed under conditions transitional between granulite and amphibolite facies. The *P–T* parameters estimated for garnet rims and matrix minerals in aluminous gneisses, which are significantly lower than the peak conditions (samples 359-3b, 348-4/2, and 361/2), can be attributed to the progressive or regressive stage of the same metamorphic event.

Note that the metabasites corresponding in composition to ferrogabbronorites (sample 362) underwent only amphibolite metamorphism at 4–5 kbar and 620–730 °C. It is necessary to study whether this fact indicates the intrusion of the metabasites after granulite metamorphism and the manifestation of the amphibolite facies metamorphism or it is the result of the dominant impact of regressive metamorphism on these rocks. It is remarkable that our measurements did not yield high pressures of 9.5–10.0 kbar for the Larba granulites, which were reported by previous researchers (Glebovitsky et al., 2009).

It is still unclear what stage (or stages) of granulite metamorphism the estimated *P–T* parameters correspond to, because high-grade metamorphism might have occurred both in the Archean and in the Paleoproterozoic. A wide age range was reported earlier for granulite metamorphism in the Dzhugdzhur–Stanovoi folded area and the Pristanovoi belt (2.1–2.6 Ga) (Glebovitsky et al., 2009). According to structural and geological data, the Neoarchean granulite facies metamorphism in the Larba block (Bibikova et al., 1984) was associated with the formation of a nappe–thrust structure in the collision setting (Glebovitsky et al., 2009).

So, the available geochronological data are not enough to estimate the time of high-grade metamorphism; moreover, it might have repeated in the study area. Therefore, further studies of metamorphic rocks are necessary. This is especially urgent with regard to the fact that metamorphic events might have occurred both in the Archean and in the Paleoproterozoic (Glebovitsky et al., 2009). In recent studies of granulite blocks of the Dzhugdzhur–Stanovoi folded area and the Pristanovoi belt, high-grade metamorphism has been dated at 2.1–2.6 Ga (Glebovitsky et al., 2009), but earlier petrological, structural, and geological data and dates of zircon extracted from garnet of the Larba block suggested Neoarchean metamorphism, 2585 ± 20 Ma (Bibikova et al., 1984). It was believed that the granulite facies metamorphism was associated with the formation of nappe–thrust structures in the collision setting at that time.

Paleoproterozoic metamorphism in the Dzhugdzhur–Stanovoi folded area (ca. 1.9 Ga) was repeatedly mentioned in earlier publications, in particular, by Glebovitsky et al. (2009). For example, the complex of parautochthonous charnockites (1880 ± 21 Ma) of the Larba block, formed at the final stage of granulite metamorphism, was also associa-

ted with collision events. In the Dambuki block, the time of granulite metamorphism was estimated by zircon dating of enderbites (1884 ± 9 Ma) and metasomatites of the granulite facies (1896 ± 15 Ma) (Glebovitsky et al., 2009). These geochronological data, which are probably correlated with our results, confirm the existence of a global system of collisional orogens and the accretion of large fragments of continental crust in the Paleoproterozoic.

Thus, the Paleoproterozoic metamorphic event dated from the shells of enderbite zircon is interpreted as a widely manifested endogenous activity on a regional and even interregional scale. The most complete information about this endogenous stage is given in a number of publications (Gladkochub et al., 2013; Donskaya et al., 2013, 2014, 2016, 2018, 2020; Donskaya and Gladkochub, 2021). In particular, three stages of collisional granitoid magmatism were established for the Siberian craton (Donskaya et al., 2020; Donskaya and Gladkochub, 2021): 1.95–2.00, 1.90–1.95, and 1.87–1.90 Ga. The time of occurrence of granulite metamorphism in the Larba block rocks coincides with the third stage of magmatism, which is well correlated with the area of collision events in the Siberian craton.

Nevertheless, it is still unclear what structures could have been involved in Paleoproterozoic collision events. Since the intrusion of enderbites was associated with Meso–Neoarchean postcollisional events, e.g., the collision of the Dzhugdzhur–Stanovoi and Olekma terranes of the Aldan Shield (other terranes had not yet formed by that time), the western part of the Aldan Shield and half of the Stanovoi area already constituted a consolidated microcontinent. What could it have collided with? If we assume a predominance of E–W rather than N–S striking motions in the Paleoproterozoic, then it is more logical to regard the Stanovoi structural suture as a shear zone rather than as a Paleoproterozoic collisional structure. These questions have not yet been answered in the framework of the obtained results and call for additional research.

CONCLUSIONS

The time of intrusion and the age of intrusive enderbites are still unclear. Judging from the cores of magmatic zircons, the magmatic stage of the formation of these rocks was ca. 2.5 Ga. The enderbites underwent high-temperature metamorphism with the formation of zircon shells in the Paleoproterozoic, ca. 1.88 Ga. Granulite metamorphism of the Larba block rocks took place under moderate-pressure conditions; there are no signs of high-pressure (>8 kbar) metamorphism. The estimated *P–T* conditions of metamorphism of aluminous gneisses correspond to the moderate-pressure granulite facies conditions (7–8 kbar, 800–850 °C). Orthopyroxene–biotite–garnet gneisses formed under conditions transitional between the granulite and amphibolite facies. Ferrous metabasites were metamorphosed at 4–5 kbar and 620–730 °C, which corresponds to the "postgranulite" (regressive) stage of metamorphism. The lowest-temperature changes are specific to the conditions of the chlorite–muscovite subfacies of the greenschist facies.

The time of granulite metamorphism must be refined, because the established multistage transformations of rocks and the presence of several mineral assemblages in metapelites and metabasites do not rule out repeated amphibolite and granulite facies metamorphism.

The Paleoproterozoic metamorphism of the Larba block coincides regionally with the third stage of collisional granitoid magmatism in the southeast of the Siberian craton.

We sincerely thank S.D. Velikoslavinskii and A.M. Larin (Institute of Precambrian Geology and Geochronology RAS, St. Petersburg) for valuable consultations during the preparation of the paper. We are also sincerely grateful to Fernando Corfu (Institute of Geology, University of Oslo, Norway), who reviewed the materials on zircon isotope dating of enderbites and provided valuable advice regarding the zircon structure and interpretation of the results. The thoughtful and supportive reviews by E.V. Sklyarov (Institute of Geosciences SB RAS, Irkutsk) and an anonymous reviewer helped to improve the manuscript.

The work was carried out with a financial support of the research project FMUW-2022-0002 of the Institute of Precambrian Geology and Geochronology RAS, St. Petersburg, by the Ministry of Education and Science of the Russian Federation.

Supplementary Materials. Table S1. Chemical compositions of minerals.

REFERENCES

Aleksandrov, I.A., Avchenko, O.V., 2002. Comparative thermobarometry of metamorphic complexes and a geodynamic model of the relationship between the Aldan and the Dzhugdzhur–Stanovoi blocks (Aldan–Stanovoi Shield). Tikhookeanskaya Geologiya 21 (5), 3–14.

Berman, R.G., 1991. Thermobarometry using multi-equilibrium calculations: a new technique, with petrological applications. Can. Mineral. 29, 833–855.

Berman, R.G., 2007. winTWQ (version 2.3): a software package for performing internally-consistent thermobarometric calculations. Geological Survey of Canada Open File 5462, doi: 10.4095/223425.

Berman, R.G., Aranovich, L.Ya., 1996. Optimized standard state and solution properties of minerals. Contrib. Mineral. Petrol. 126 (1–2), 1–24, doi: 10.1007/s004100050233.

Berman, R.G., Aranovich, L.Ya., Rancourt, D.G., Mercier, D.G., 2007. Reversed phase equilibrium constraints on the stability of Mg–Fe–Al biotite. Am. Mineral. 92, 139–150, doi: 10.2138/am.2007.2051.

Bibikova, E.V., Shul'diner, V.I., Gracheva, T.V., Panchenko I.V., Makarov, V.A., 1984. The isotopic age of granulites in the west of the Stanovoi area. Dokl. Akad. Nauk SSSR 275 (6), 1471–1474.

Black, L.P., Kamo, S.L., Allen, C.M., Davis, D.W., Aleinikoff, J.N., Valley, J.W., Mundil, R., Campbell, I.H., Korsch, R.J., Williams, I.S., Foudoulis, C., 2004. Improved $^{206}Pb/^{238}U$ microprobe geochronology by the monitoring of a trace-element-related matrix effect; SHRIMP, ID-TIMS, ELA-ICP-MS and oxygen isotope documentation for a series of zircon standards. Chem. Geol. 205, 115–140, doi: 10.1016/j.chemgeo.2004.01.003.

Buchko, I.V., Sorokin, A.A., 2010. Neoarchean ultramafic–mafic magmatism in the Dzhugdzhur-Stanovoi superterrane, in: Geology and Minerageny of Transbaikalia: Proceedings of the Research and Development Conference [in Russian]. Chitageols''emka, Chita, pp. 103–105.

Buchko, I.V., Salnikova, E.B., Kotov, A.B., Sorokin, A.P., Larin, A.M., Velikoslavinskii, S.D., Yakovleva, S.Z., Plotkina, Yu.V., 2008. Age and tectonic position of the Khorogochi gabbro-anorthosite massif (Dzhugdzhur–Stanovoi superterrane). Dokl. Earth Sci. 423, 1312–1315, doi: 10.1134/S1028334X08080291.

Dolivo-Dobrovolsky, D.V., 2006a. TWQ_Comb: the program for automatic generation of all possible combinations of selected mineral analyses and for their processing by CMP.EXE and TWQ.EXE programs (from the TWQ package of R.G. Berman et al.) running in the batch mode, Version 1.3.0.2, url: dimadd.ru/en/Programs/twqcomb.

Dolivo-Dobrovolsky, D.V., 2006b. TWQ_View: the program for viewing and work with diagrams generated by the TWQ program of R.G. Berman (1991) used for multi-equilibrium geothermobarometry, Version 1.3.0.1, url: dimadd.ru/en/Programs/twqview.

Donskaya, T.V., 2020. Assembly of the Siberian Craton: Constraints from Paleoproterozoic granitoids. Precambrian Res. 348, 105869, doi: 10.1016/j.precamres.2020.105869.

Donskaya, T.V., Gladkochub, D.P., 2021. Post-collisional magmatism of 1.88–1.84 Ga in the southern Siberian Craton: An overview. Precambrian Res. 367, 106447, doi: 10.1016/j.precamres.2021.106447.

Donskaya, T.V., Gladkochub, D.P., Mazukabzov, A.M., Presnyakov, S.L., Bayanova, T.B., 2013. Paleoproterozoic granitoids of the Chuya and Kutima complexes (southern Siberian craton): age, petrogenesis, and geodynamic setting. Russ. Geol. Geophys. 54 (3), 283–296, doi: 10.1016/j.rgg.2013.02.004.

Donskaya, T.V., Gladkochub, D.P., Mazukabzov, A.M., Wingate, M.T.D., 2014. Early Proterozoic postcollisional granitoids of the Biryusa block of the Siberian craton. Russ. Geol. Geophys 55 (7), 812–823, doi: 10.1016/j.rgg.2014.06.002.

Donskaya, T.V., Gladkochub, D.P., Mazukabzov, A.M., Lepekhina, E.N., 2016. Age and sources of the Paleoproterozoic premetamorphic granitoids of the Goloustnaya block of the Siberian craton: geodynamic applications. Petrology 24 (6), 543–561, doi: 10.1134%2FS0869591116050040.

Donskaya, T.V., Mazukabzov, A.M., Gladkochub, D.P., 2018. Petrogenesis and structural position of the Early Proterozoic charnockites of the Tatarnikovsky massif in the South Siberian post-collisional magmatic belt of the Siberian craton. Geodynamics & Tectonophysics 9 (2), 391–412, doi: 10.5800/GT-2018-9-2-0352.

Dzevanovskii, Yu.K., 1958. Geology of the western margin of the Stanovoi Ridge. Byulleten' VSEGEI, No. 1, 21–27.

Friend, C.R.L., Kinny, P.D., 1995. New evidence for protolith ages of Lewisian granulites, northwest Scotland. Geology 23, 1027–1030, doi: 10.1130/0091-7613(1995)023%3C1027:NEFPAO%3E2.3.CO;2.

Gladkochub, D.P., Pisarevsky, S.A., Mazukabzov, A.M., Söderlund, U., Sklyarov, E.V., Donskaya, T.V., Ernst, R.E., Stanevich, A.M., 2013. The first evidence of Paleoproterozoic late-collision basite magmatism in the near-Sayan salient of the Siberian craton basement. Dokl. Earth Sci. 450 (2), 583–586, doi: 10.1134/S1028334X13060019.

Glebovitskii, V.A. (Ed.), 2005. The Early Precambrian of the Baltic Shield [in Russian]. Nauka, St. Petersburg.

Glebovitsky, V.A., Kotov, A.B., Salnikova, E.B., Larin, A.M., Velikoslavinsky, S.D., 2009. Granulite complexes of the Dzhugdzhur–Stanovoi Fold Region and the Peristanovoi Belt: age, formation conditions, and geodynamic settings of metamorphism. Geotectonics 43, 253–263, doi: 10.1134/S0016852109040013.

Glukhovskii, M.Z., Sintserova, E.A., 1979. Metamorphic formations in the zone of junction of the Aldan Shield and the Dzhugdzhur–Stanovoi fold area (as applied to the problem of the Stanovoi Complex), in: Precambrian Complexes of the Baikal–Amur Mainline Zone [in Russian]. DVNTs AN SSSR, Vladivostok, pp. 72–90.

Green, E.C.R., White, R.W., Diener, J.F.A., Powell, R., Holland, T.J.B., Palin, R.M., 2016. Activity–composition relations for the calculation of partial melting equilibria in metabasic rocks. J. Metamorph. Geol. 34, 845–869, doi: 10.1111/jmg.12211.

Holland, T.J.B., Powell, R., 2011. An improved and extended internally consistent thermodynamic dataset for phases of petrological interest, involving a new equation of state for solids. J. Metamorph. Geol. 29, 333–383, doi: 10.1111/j.1525-1314.2010.00923.x.

Kastrykina, V.M., 1983. Metamorphism in the central part of the Dzhugdzhur–Stanovoi folded area, in: Precambrian Metamorphism in the Baikal–Amur Mainline Region [in Russian]. Nauka, Leningrad, pp. 140–163.

Korzhinskii, D.S., 1936. Petrology of the Archean Complex of the Aldan Plate. Proceedings of TsNIGRI [in Russian]. ONTI NKTP SSSR, Leningrad, Moscow, Issue 86.

Kotov, A.B., Larin, A.M., Salnikova, E.B., Velikoslavinskii, S.D., Glebovitskii, V.A., Sorokin, A.A., Yakovleva, S.Z., Anisimova, I.V., 2014. Early Cretaceous collisional granitoids of the Drevnestanovoi complex from the Selenga–Stanovoi superterrane of the Central Asian mobile belt. Dokl. Earth Sci. 456 (2), 649–654, doi: 10.1134/S1028334X14060154.

Kozyreva, I.V., Avchenko, O.V., Mishkin, M.A., 1985. Deep Metamorphism of the Late Archean Volcanic Belts [in Russian]. Nauka, Moscow.

Kusiak, M.A., Dunkley, D.J., Wirth, R., Whitehouse, M.J., Wilde, S.A., Marquard, K., 2015. Metallic lead nanospheres discovered in ancient zircons. PNAS 112, 4958–4963, doi: 10.1073/pnas.1415264112.

Kusiak, M.A., Kovaleva, E., Wirth, R., Klötzli, U., Dunkley, D.J., Yi, K., Lee, S., 2019. Lead oxide nanospheres in seismically deformed zircon grains. Geochim. Cosmochim. Acta 262, 20–30, doi: 10.1016/j.gca.2019.07.026.

Larin, A.M., Kotov, A.B., Salnikova, E.B., Glebovitskii, V.A., Sukhanov, M.K., Yakovleva, S.Z., Kovach, V.P., Berezhnaya, N.G., Velikoslavinskii, S.D., Tolkachev, M.D., 2006. The Kalar Compex, Aldan–Stanovoi shield, an ancient anorthosite–mangerite–charnockite–granite association: geochronologic, geochemical, and isotopic-geochemical characteristics. Petrology 14, 2–20, doi: 10.1134/S0869591106010024.

Larin, A.M., Kotov, A.B., Velikoslavinskii, S.D., Salnikova, E.B., Kovach, V.P., 2012. Early Precambrian *A*-granitoids in the Aldan Shield and adjacent mobile belts: sources and geodynamic environments. Petrology 20, 218–239, doi: 10.1134/S0869591112030034.

Lieberman, J., Petrakakis, K., 1991. TWEEQU thermobarometry; analysis of uncertainties and applications to granulites from western Alaska and Austria. Can. Mineral. 29, 857–887.

Ludwig, K.R., 2005. SQUID 1.13a. A user's manual. A geochronological toolkit for Microsoft Excel. Berkeley Geochronology Center Special Publication No 2.

Ludwig, K.R., 2012. User's manual for Isoplot 3.75. A geochronological toolkit for Microsoft Excel. Berkeley Geochronology Center Special Publication No 5.

Moskovchenko, N.I., Semenov, L.P., Verkhalo-Uzkii, V.N., 1985. Granulite complexes of the Stanovoi folded area, in: The Early Precambrian of the Aldan Massif and Its Framing [in Russian]. Nauka, Leningrad, pp. 121–144.

Moskovchenko, N.I., Ovchinnikova, G.V., Kastrykina, V.M., 1993. High-pressure granulites of East Siberia in terms of Archaean and Proterozoic evolution. Precambrian Res. 63, 473–491, doi: 10.1016/0301-9268(93)90017-V.

Salnikova, E.B., Kotov, A.B., Belyatsky, B.V., Yakovleva, S.Z., Morozova, I.M., Berezhnaya, N.G., Zagornaya, N.Yu., 1997. U–Pb age of granitoids in the junction zone between the Olekma granite–greenstone and Aldan granulite–gneiss terranes. Stratigr. Geol. Correl. 5 (2), 101–109.

Salnikova, E.B., Larin, A.M., Kotov, A.B., Glebovitskii, V.A., Sukhanov, M.K., Yakovleva, S.Z., Kovach, V.P., Berezhnaya, N.G., Tolkachev, M.D., 2004. The Kalar anorthosite–charnokite complex of

the Aldan–Stanovoi Shield: age and tectonic implications. Stratigr. Geol. Correl. 12 (3), 221–228.

Sedova, I.S., Glebovitskii, V.A., 1985. Granite formation under conditions of amphibolite facies in the zone of rocks of the Stanovoi Complex, in: The Early Precambrian of the Aldan Massif and Its Framing [in Russian]. Nauka, Leningrad, pp. 92–121.

Velikoslavinskii, S.D., Kotov, A.B., Salnikova, E.B., Larin, A.M., Sorokin, A.A., Sorokin, A.P., Kovach, V.P., Tolmacheva, E.V., Gorokhovskii, B.M., 2011. Age of the Ilikan Sequence from the Stanovoi Complex of the Dzhugdzhur–Stanovoi Superterrane, Central-Asian Foldbelt. Dokl. Earth Sci. 438 (1), 612–616, doi: 10.1134/S1028334X11050400.

Velikoslavinskii, S.D., Kotov, A.B., Kovach, V.P., Tolmacheva, E.V., Sorokin, A.A., Salnikova, E.B., Larin, A.M., Zagornaya, N.Yu., Wang, K.L., Chung, S.-L., 2017. Age and tectonic position of the Stanovoi metamorphic complex in the eastern part of the Central Asian Foldbelt. Geotectonics 51 (4), 341–352, doi: 10.1134/S0016852117040070.

Warr, L.N., 2021. IMA–CNMNC approved mineral symbols. Mineral. Mag. 85, 291–320, doi: 10.1180/mgm.2021.43.

Wiedenbeck, M., Allé, P., Corfu, F., Griffin, W.L., Meier, M., Oberli, F., von Quadt, A., Roddick, J.C., Spiegel, W., 1995. Three natural zircon standards for U–Th–Pb, Lu–Hf, trace element and REE analysis. Geostand. Newslett. 19, 1–3, doi: 10.1111/j.1751-908X.1995.tb00147.x.

Williams, I.S., 1997. U-Th-Pb geochronology by ion microprobe, in: McKibben, M.A., Shanks III, W.C., Ridley, W.I. (Eds.), Applications of Microanalytical Techniques to Understanding Mineralizing Processes. Rev. Econ. Geol. 7, pp. 1–35, doi: 10.5382/Rev.07.

Xiang, H., Connolly, J.A.D., 2022. GeoPS: An interactive visual computing tool for thermodynamic modelling of phase equilibria. J. Metamorph. Geol. 40, 243–255, doi: 10.1111/jmg.12626.